QUANTIFICATION OF REGIONAL PERFUSION, SHUNT FRACTION AND VENTILATION USING POSITRON EMISSION TOMOGRAPHY: A NONLINEAR TRACER KINETICS MODEL

by

Gaetano Giovanni Galletti

B.S. Mechanical Engineering
Loyola Marymount University, 1995

Submitted to the Department of Mechanical Engineering in partial fulfillment of the requirements for the degree of

Master of Science in Mechanical Engineering

at the

MASSACHUSETTS INSTITUTE OF TECHNOLOGY

June 1998

Author.....
Department of Mechanical Engineering
May 8, 1998

Certified by.....
Jose G. Venegas
Assistant Professor, Harvard Medical School
Thesis Supervisor

Accepted by.....
Ain A. Sonin
Chairman, Departmental Committee on Graduate Students

QUANTIFICATION OF REGIONAL PERFUSION, SHUNT FRACTION AND VENTILATION USING POSITRON EMISSION TOMOGRAPHY: A NONLINEAR TRACER KINETICS MODEL

by

Gaetano Giovanni Galletti

Submitted to the Department of Mechanical Engineering
on May 8, 1998 in partial fulfillment of the
requirements for the degree of
Master of Science in Mechanical Engineering

ABSTRACT

Quantification of gas exchange in the lung using Positron Emission Tomography (PET) allows validation of mechanistic hypotheses regarding the local regulation of pulmonary function. We have developed a nonlinear lumped-parameter model to simulate the regional kinetics of the tracer $^{13}N_2$ as measured by PET following a rapid intravenous injection of a bolus of $^{13}N_2$ in saline solution. The model is made of a compartment representing the right heart and pulmonary vasculature through which the tracer is mixed and diluted in blood. From this compartment, blood is distributed to two compartments for each defined region of interest (ROI). One lumps all aerated alveolar units, and the other lumps all atelectatic, edematous or fluid filled alveolar units with no gas content. Differential equations of the model were solved numerically and the parameters estimated using gradient-descent search algorithms. The model was applied to PET data from supine sheep to study the effects of partial liquid ventilation (PLV) in bilaterally surfactant-depleted lungs. Images were divided in three ROI's along the vertical axis: nondependent, middle and dependent. It was concluded that PLV reduces shunt in the surfactant-depleted lung.

In a second chapter, a new methodology to estimate the fractal dimension of two-dimensional images is described. The method was applied to PET images of perfusion obtained from normal dogs. A relationship between the fractal dimension and Power Spectral Density was studied, leading to new insights for the physical interpretation of the fractal dimension.

Thesis Supervisor: Jose G. Venegas, Ph.D.
Title: Assistant Professor, Harvard Medical School

ACKNOWLEDGEMENTS

I would like to acknowledge the unending support of my family, without whom the opportunity to study at MIT would have been unattainable. I am particularly thankful to my mother and father for continuously stressing the importance and merit of a graduate education, and for their faithful confidence in my academic ability.

The opportunity to work and study in the laboratory of Dr. Jose G. Venegas at the Massachusetts General Hospital is greatly appreciated. I am confident I will benefit from the knowledge and experience he has passed down to me as an academic/research advisor, mentor, role model and friend throughout the duration of my graduate career. I am notably grateful for his persistent emphasis in the fact that thinking is the important element in the craft of problem solving.

The diversified nature of this project allowed me to interface with professionals in the medical field. The help I received from Dr. Donna Beth Willey-Courand from the Pediatrics-Pulmonary Division and Dr. R. Scott Harris from the Pulmonary and Critical Care Division of the Massachusetts General Hospital was essential for my comprehension of the biological and physiological aspects of my project.

My final gratitude is expressed to Keiko Foojiwawa of the Harvard-MIT Health Sciences and Technology Department and Leslie Regan of the MIT Mechanical Engineering Department for managing the administrative aspects of my matriculation at MIT and for their unparalleled dedication to easing the stressfulness of the graduate experience.

DEDICATION

For My Family

Pa, Ma, Phil and Mare

You are the balance in my life. I love you.

CONTENTS

CHAPTER 1. DEVLOPMENT OF A NONLINEAR TRACER KINETICS MODEL FOR QUANTITATIVE ANALYSIS OF POSITRON EMISSION TOMOGRAPHY FUNCTIONAL IMAGES

CHAPTER 2. FRACTAL ANALYSIS OF POSITRON EMISSION TOMOGRAPHY IMAGES OF PULMONARY BLOOD FLOW

LIST OF FIGURES

CHAPTER 1. DEVLOPMENT OF A NONLINEAR TRACER KINETICS MODEL FOR QUANTITATIVE ANALYSIS OF POSITRON EMISSION TOMOGRAPHY FUNCTIONAL IMAGES

Figure 4. Fractal plot for the low-pass filtering method of the natural logarithm of the *cov* vs. the natural logarithm of the normalized inverse corner frequency of the filter. Method was applied to one hundred random noise images cast in the shape and size of a typical dog lung cross section. The average ln(*cov*%) for the one hundred images was calculated per low-pass filter corner frequency (f_c). Error bars indicate ± standard deviation for each data point. A linear regression fit through the data in this figure yielded D of 1.5045 with an R^2 of 0.9998.

78

Figure 5. Synthetic fractal image of figure (1) processed with the low-pass filtering method (*left column*) and conventional method (*right column*) with increasing resolution scale (top to bottom). For the low-pass filtering method, the image was filtered with f_c of $0.492f_N$, $0.2265f_N$ and $0.0498f_N$, respectively. For the conventional method, side lengths of the grouping squares in number of voxels were 4, 8 and 32 voxels, respectively.

80

Figure 6. Fractal plot for the conventional method of the natural logarithm of the *cov* vs. the natural logarithm of the square root of the number of voxels in a square piece applied to the synthetic fractal image of figure (1). Three different grids were used: proper grid (◆), misregistered grid (■), and a misaligned grid (●).

81

Figure 7. Fractal plot for the low-pass filtering method of the natural logarithm of the *cov* vs. the natural logarithm of the normalized inverse corner frequency of the filter. Method was applied to the synthetic fractal image of figure (1) for an original image (◆) and one displaced by one voxel by padding with zeros (●). The two best-fit lines coincide exactly, irrespective of zero padding.

81

Figure 8. Composite fractal plot for the low-pass filtering method of the natural logarithm of the *cov* vs. the natural logarithm of the normalized inverse corner frequency of the filter for six normal dogs lying supine. Note that inflection towards a plateau occurs at the same spatial frequency for all dogs, which corresponds to the intrinsic spatial resolution of the PET camera.

83

Figure 9. Fractal plot for the low-pass filtering method of the natural logarithm of the *cov* versus the natural logarithm of the normalized inverse corner frequency of the filter. Method was applied to a random noise image that was corrected for edge-smearing (normalization by an equivalently filtered unity mask) at each level of resolution (●). The expected linearity (R^2 = 0.9997) and fractal dimension (D = 1.53) are calculated from the best-fit line. Without correction for smeared edges (■), increasing resolution scale introduces artifactual heterogeneity that causes deviation from linearity (R^2 = 0.9002) and an erroneous fractal dimension (D = 1.25).

87

LIST OF TABLES

CHAPTER 1. DEVLOPMENT OF A NONLINEAR TRACER KINETICS MODEL FOR QUANTITATIVE ANALYSIS OF POSITRON EMISSION TOMOGRAPHY FUNCTIONAL IMAGES

CHAPTER 2. FRACTAL ANALYSIS OF POSITRON EMISSION TOMOGRAPHY IMAGES OF PULMONARY BLOOD FLOW

CHAPTER 1

DEVELOPMENT OF A NONLINEAR TRACER KINETICS MODEL FOR QUANTITATIVE ANALYSIS OF POSITRON EMISSION TOMOGRAPHY FUNCTIONAL IMAGES

1. INTRODUCTION

Positron Emission Tomography (PET) enables accurate, non-invasive and quantitative measurements of the regional distribution of a positron-emitting isotope tracer within the lung in well-defined thoracic volume elements (voxels). Raw PET image data has to be analyzed using mathematical models to derive physiological parameters from the distribution and kinetics of the radiolabeled tracers. In the case of pulmonary functional imaging, identified regional physiological parameters such as alveolar ventilation ($\dot{V}_A$) and perfusion ($\dot{Q}$) can be integrated with other global physiologic data to test mechanistic hypotheses about the local regulation of pulmonary function in health and disease.

Rhodes et al. pioneered the topographic measurements of the $\dot{V}_A / \dot{Q}$ ratio with PET during a constant infusion of $^{13}N_2$ gas dissolved in saline solution [6][7]. The method was recently refined utilizing a single bolus injection during apnea and respiratory gating during the washout period, and an improved system to optimize the labeling with $^{13}N_2$ into saline [5]. The refined imaging protocol required that during apnea, at functional residual capacity, a bolus of the $^{13}N_2$-labeled saline be infused intravenously. Simultaneously with the beginning of infusion, a sequence of images was initiated and continuously collected for the duration of the apneic period. Mechanical ventilation was

then restarted at the end of apnea, and a sequence of washout images was collected. The validity of this method rests on the assumption that, upon its arrival to the pulmonary capillary vessels, most of the tracer migrates to the alveolar airspace where it remains during apneic imaging. In the normal lung, activity therefore climbs towards its peak level as tracer arrives and diffuses into the alveolar airspace and approximately stabilizes at that peak level as tracer equilibrates with alveolar airspace. Its reabsorbtion into pulmonary venous blood and body tissue and subsequent removal from the imaging region are minimal by virtue of the low partition coefficient for $^{13}N_2$ between air and blood. Thus, distribution of the tracer at the voxel level is proportional to local perfusion and the images collected during apnea can be used to assess regional perfusion ($\dot{Q}_R$). Washout image data can be used directly to assess regional ventilation ($\dot{V}_A$) since, in the normal lung, the dominant mechanism of tracer removal during the washout period should be ventilation.

In the injured or diseased lung, activity climbs towards its peak during apnea and is then removed from the imaging region by its reabsorbtion into the blood reflecting intrapulmonary shunt blood flow ($\dot{Q}_S$). If the time constant (τ_S) characterizing apneic tracer removal by shunt is much shorter than the duration of apnea such that the activity level reaches a plateau, then this stabilized activity level should be proportional to regional blood flow to aerated alveolar units ($\dot{Q}_A$). Also, the dominant mechanism of tracer removal during the washout should be ventilation. If activity continues to be removed by shunt blood flow beyond the apneic period into the washout phase, then activity is removed from the imaging region during the washout period via two

competing mechanisms: shunt in atelectatic alveolar units and ventilation in aerated alveolar units. Washout data therefore cannot be used directly to assess regional ventilation. Furthermore, the peak regional activity level that is observed with the PET functional image data from diseased or injured lungs might not reflect regional perfusion. This is because activity can be removed from the imaging region by shunt blood flow simultaneously with the injection, and because PET instrumentation does not acquire instantaneous radioactive decay events but rather averages them for a finite imaging period.

In this chapter, we describe the development of a lumped-parameter two-compartment model to simulate the tracer kinetics data measured with PET following a bolus injection of $^{13}N_2$-labeled saline solution. This model simulates the tracer transit time from the point of injection to the alveoli, equilibration of tracer concentration between alveolar airspace and pulmonary blood, and alveolar removal of the tracer by shunt blood flow and ventilation. A nonlinear system identification technique was applied to PET imaging data to extract model parameters from surfactant deficient lungs before and after partial liquid ventilation (PLV).

2. MATERIALS AND METHODS

2.1. Model

The general structure of the model developed is schematically shown in figure (1). Radiolabeled saline is injected peripherally (infusion flow rate $\dot{Q}_I$, infusate specific activity C_I) and mixed with venous blood in the heart and the pulmonary arterial tree resulting in a time-dependent pulmonary arterial blood concentration, $C_{PA}(t)$. The kinetics of this compartment are lumped into a well-mixed chamber of volume V_H

through which the total cardiac output ($\dot{Q}_T$) flows. The convective delay from the injection site to the alveolar gas-exchanging interface is lumped into a single time delay (Δt_{TD}). The time-shifted $C_{PA}(t)$ signal is used as the input to three ROI's: dependent (D), middle (M) and nondependent (ND). The blood flow rates to these three ROI's are $\dot{Q}_{R,D}$, $\dot{Q}_{R,M}$ and $\dot{Q}_{R,ND}$, respectively. Alveolar units in each ROI are lumped into one of two well-mixed compartments that are assumed to behave independently of each other. One compartment corresponds to aerated alveolar units with a tracer volume of distribution V_A and specific alveolar ventilation $s\dot{V}_A$. A second "shunt" compartment lumps all atelectatic, edematous or fluid filled alveolar units with no gas content. This compartment has a tracer volume of distribution V_S and concentration $C_S(t)$. By continuity, regional perfusion is the sum of the blood flows: $\dot{Q}_R = \dot{Q}_A + \dot{Q}_S$. Regional tracer content is: $V_A C_A(t) + V_S C_S(t)$. This signal is used as input for a PET camera block that simulates the camera's signal averaging during image collection yielding discrete data points of average tracer content per image ($\overline{C_i}$) for each ROI during the corresponding imaging period.

Modeling assumptions and differential equations describing the system dynamics are described in the following subsections.

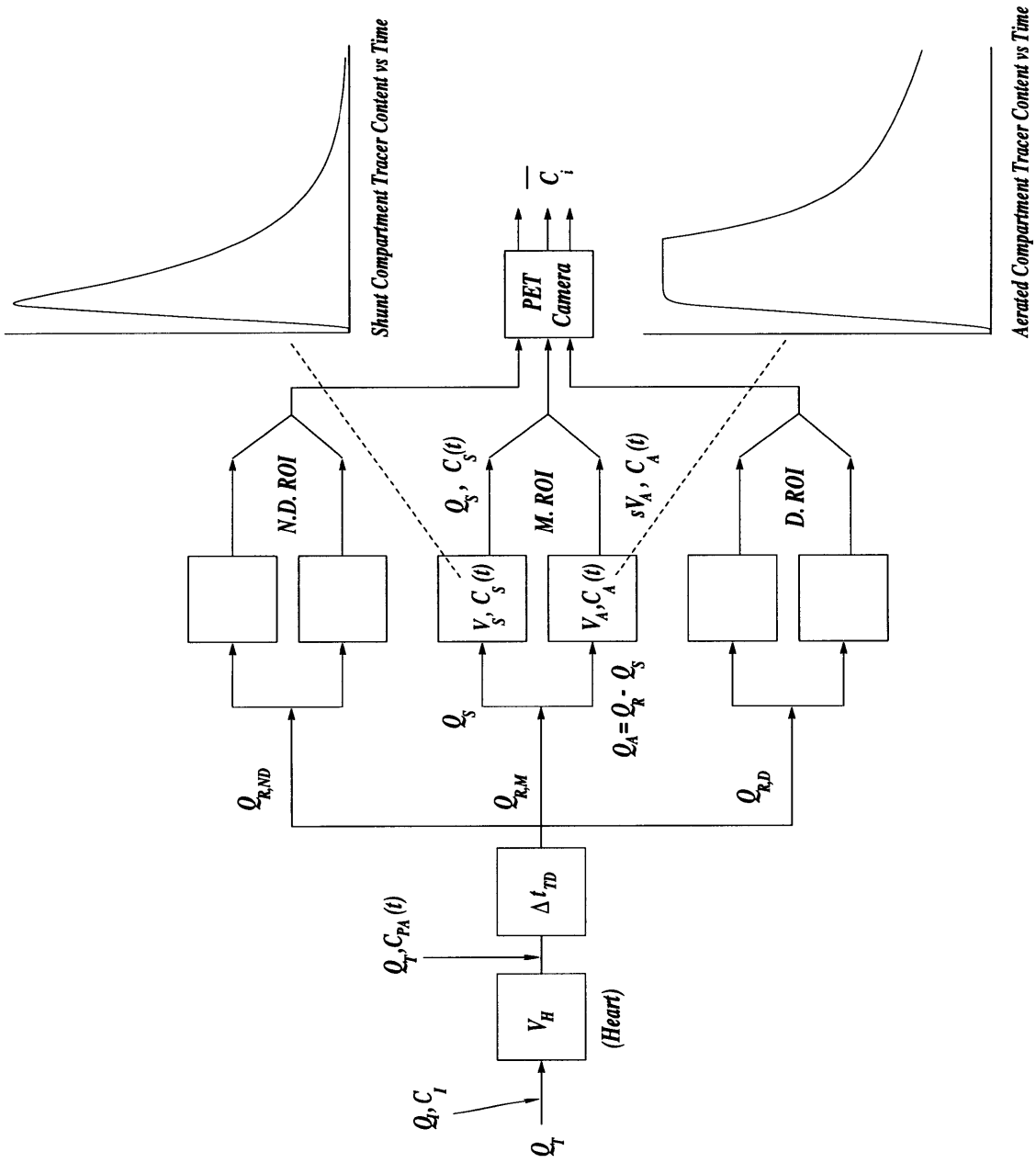

Figure 1. Model schematic showing an initial compartment with effective mixing volume V_H. Its dynamics represent the mixing and dilution of the IV-injected $^{13}N_2$-labeled saline in pulmonary arterial blood. Its output concentration function $C_{PA}(t)$, time-shifted by Δt_{TD}, is the input to the imaged section of the lung, which consists of 3 ROI's: nondependent (*ND*), middle (*M*) and dependent (*D*). Each ROI is comprised of 2 compartments: aerated (*A*) and shunt (*S*). Time-dependent tracer content following the injection is associated with each compartment in an ROI, and described by its differential equation. Dashed lines emanating from the middle ROI point to representative tracer content curves. Regional tracer content is the sum of the aerated and shunt compartment tracer contents, and represents the signal continuously integrated and then averaged by the PET camera yielding average tracer content ($\overline{C_i}$) per ROI.

2.1.1. Modeling Assumptions

Modeling assumptions include:

1. Each compartment in the model denotes a potential space in which uniform distribution of the tracer is assumed.
2. Pulmonary blood flow and ventilation are assumed to be invariant and continuous during the measurement period (in reality, blood flow and ventilation are pulsatile processes; the assumption therefore treats these physiologic processes as quasi-continuous). Since the measurement times (i.e., PET scan lengths) are much longer than the cycle periods, this assumption results in the calculation of cyclic averages of the processes over the lengths of the scans.
3. Following an intravenous bolus injection of $^{13}N_2$-labeled saline, the tracer injected distributes at the alveolar level in proportion to local perfusion.
4. Behaviors of user-defined ROI's are independent of one another, and the effects of tracer mass diffusion between adjacent ROI's due to concentration gradients and cardiogenic oscillations during apnea are neglected.

2.1.2. Right Heart and Pulmonary Artery and Vasculature

The right heart and pulmonary artery and vasculature are lumped into a well-mixed chamber of volume V_H with two inputs and one output. Inflow of tracer comes from $^{13}N_2$-labeled saline with specific activity C_I and flow rate $\dot{Q}_I$, and from tracer present in recirculating blood with specific activity C_R and flow rate $\dot{Q}_T$. Outflow of tracer is by convection of blood flow from the right ventricle of the heart with concentration $C_{PA}(t)$. Conservation of mass applied to a control volume surrounding the lumped heart and pulmonary blood vessels requires that the effective mixing volume (V_H)

multiplied by the rate of change of tracer concentration in the heart and pulmonary blood vessels ($\frac{dC_H(t)}{dt}$) must be equal to the tracer inflow by externally infused radiolabeled saline ($\dot{Q}_I C_I$) and recirculation ($\dot{Q}_T C_R$) minus tracer outflow by pulmonary arterial blood ($(\dot{Q}_T + \dot{Q}_I) C_{PA}(t)$).

$$V_H \frac{dC_H(t)}{dt} = \dot{Q}_I C_I - (\dot{Q}_T + \dot{Q}_I) C_{PA}(t) + \dot{Q}_T C_R \qquad (1)$$

where
V_H = effective mixing volume, mL,
$C_H(t)$ = radioactive concentration of tracer in the heart and pulmonary blood vessels, nCi/mL,
$\dot{Q}_I$ = $^{13}N_2$-labeled saline infusion flow rate, mL/sec,
C_I = infusate specific activity, nCi/mL,
$\dot{Q}_T$ = total cardiac output, mL/sec,
$C_{PA}(t)$ = radioactive concentration of tracer in pulmonary arterial blood, nCi/mL, and
C_R = tracer activity of recirculating blood, nCi/mL.

Assuming the heart is a well-mixed chamber, $C_H(t)$ in equation (1) can be replaced by $C_{PA}(t)$. Furthermore, cardiac output in our experimental studies is typically greater than 16.67 mL/sec, and is therefore at least five times larger than the infusion flow rate of 3.33 mL/sec (i.e., $\dot{Q}_T >> \dot{Q}_I$). Using these approximations in equation (1), we have that:

$$V_H \frac{dC_{PA}(t)}{dt} \approx \dot{Q}_I C_I - \dot{Q}_T C_{PA}(t) + \dot{Q}_T C_R \qquad (2)$$

Each alveolus has a unique tracer transport delay that depends on the pulmonary arterial tree path volume and local blood flow. The model lumps the tracer transport delay for all voxels in the ROI into a single time delay (Δt_{TD}), accounting for the transport delay between the injection site and the ROI. The function of the transport delay block in figure (2) is to shift the solution to equation (2) $C_{PA}(t)$ by Δt_{TD}.

2.1.3. Aerated Compartment

The aerated compartment represents the sum of all aerated alveolar units participant in gas exchange. Inflow of tracer is the fraction of regional blood flow distributed to the compartment with concentration $C_{PA}(t)$. Local tracer removal occurs by two mechanisms: 1) pulmonary venous blood convection at a concentration $C_{VB,A}(t)$ and 2) alveolar gas ventilation at a concentration $C_A(t)$. By conservation of mass, the compartment's volume of distribution (V_A) multiplied by the rate of change of tracer concentration ($\frac{dC_A(t)}{dt}$) must equal the inflow of tracer ($\dot{Q}_A C_{PA}(t)$) minus the removal of tracer by pulmonary venous blood outflow ($\dot{Q}_A \lambda_A C_A(t)$) and ventilation ($\dot{V}_A C_A(t)$).

$$V_A \frac{dC_A(t)}{dt} = \dot{Q}_A C_{PA}(t) - \dot{Q}_A \lambda_A C_A(t) - \dot{V}_A C_A(t) \qquad (3)$$

where

V_A = aerated compartment volume of distribution, mL,
$C_A(t)$ = radioactive concentration of tracer in the aerated compartment, nCi/cm^3,

$\dot{Q}_A$ = portion of regional blood flow to the aerated compartment, mL/sec,

$\lambda_A \equiv \frac{C_{VB,A}}{C_A}$ = partition coefficient between blood and air for $^{13}N_2$, and

$\dot{V}_A$ = effective alveolar ventilation flow rate, mL/sec.

It is important to note that the volume of distribution for the tracer (V_A) is not the same as the volume of gas in the respective ROI. As explained by Schuster [10], the volume of distribution of the tracer depends on the number of alveolar units that are perfused. Since regions of aerated lung tissue may not be perfused with the labeled blood, the volume of the gas in the region may be larger than the volume of distribution of the compartment. Secondly, the partition coefficient (λ_A) relates the tracer concentration at equilibrium of the end-capillary venous blood $C_{VB,A}(t)$ and the concentration in the aerated alveoli $C_A(t)$. The partition coefficient λ_A between air and blood is taken as 0.018 (1.8%), reflecting the insolubility of $^{13}N_2$ in water.

Equation (3) was rewritten for tracer content in the compartment, given by the product of V_A and $C_A(t)$. Moving V_A inside the derivative on the left of equation (3) and rewriting the $\dot{Q}_A$ in terms of $\dot{Q}_R$ and $\dot{Q}_T$ yields:

$$\frac{d}{dt}[V_A C_A(t)] = \dot{Q}_T \left(\frac{\dot{Q}_R}{\dot{Q}_T}\right)\left(\frac{\dot{Q}_A}{\dot{Q}_R}\right) C_{PA}(t) - \frac{[V_A C_A(t)]}{\tau_A} - \left(s\dot{V}_A\right)[V_A C_A(t)] \quad (4)$$

where $\tau_A = \frac{V_A}{\dot{Q}_A \lambda_A}$ and $s\dot{V}_A = \frac{\dot{V}_A}{V_A}$, the specific alveolar ventilation. The inverse of τ_A is a transport rate constant representing the fraction of the total amount of tracer leaving the compartment per unit time. During apnea, tracer removal from the aerated compartment corresponds to the pulmonary venous blood outflow term $\dot{Q}_A \lambda_A C_A(t)$ in equation (3). Thus, τ_A can be approximated by fitting a single exponential to the apneic tracer kinetics data from a normal, gas ventilated lung. Fitted τ_A's are typically greater than 500

seconds, and therefore at least eight times longer than the 60-second apneic simulation period. It is a reasonable modeling simplification therefore to assume this rate constant $(\frac{1}{\tau_A})$ to be zero, reducing equation (4) to:

$$\frac{d}{dt}[V_A C_A(t)] = \dot{Q}_T \left(\frac{\dot{Q}_R}{\dot{Q}_R}\right)\left(\frac{\dot{Q}_A}{\dot{Q}_R}\right) C_{PA}(t) - \left(s\dot{V}_A\right)[V_A C_A(t)] \qquad (5)$$

The blood flow to an ROI is the sum of the blood flows to the aerated and shunt compartments: $\dot{Q}_R = \dot{Q}_A + \dot{Q}_S$. Substituting into equation (5) provides the differential equation used in the model.

$$\frac{d}{dt}[V_A C_A(t)] = \dot{Q}_T \left(\frac{\dot{Q}_R}{\dot{Q}_T}\right)\left(1 - \frac{\dot{Q}_S}{\dot{Q}_R}\right) C_{PA}(t) - \left(s\dot{V}_A\right)[V_A C_A(t)] \qquad (6)$$

Three parameters in this equation need to be identified: $\frac{\dot{Q}_R}{\dot{Q}_T}, \frac{\dot{Q}_S}{\dot{Q}_R}$, and $s\dot{V}_A$. $\frac{\dot{Q}_R}{\dot{Q}_T}$ is the regional perfusion expressed as a fraction of total cardiac output. $\frac{\dot{Q}_S}{\dot{Q}_R}$ is the regional shunt blood flow expressed as a fraction of the regional perfusion. $s\dot{V}_A$ is the specific alveolar ventilation.

2.1.4. Shunt Compartment

Intrapulmonary shunt refers to deoxygenated blood that enters the pulmonary arterial circulation without passing through ventilated alveolar units of the lung. Inflow of tracer into the shunt compartment is a fraction of regional blood flow with concentration $C_{PA}(t)$. Local tracer removal occurs by a single mechanism: pulmonary venous blood convection with concentration $C_{VB,S}(t)$. Conservation of mass applied to this compartment requires that the volume of distribution (V_S) multiplied by the rate of change of tracer concentration ($\frac{dC_S(t)}{dt}$) must be equal to the inflow of tracer to this compartment ($\dot{Q}_S C_{PA}(t)$) minus the removal of tracer by pulmonary venous blood outflow ($\dot{Q}_S \lambda_S C_S(t)$).

$$V_S \frac{dC_S(t)}{dt} = \dot{Q}_S C_{PA}(t) - \dot{Q}_S \lambda_S C_S(t) \tag{7}$$

where

V_S = shunt compartment volume of distribution, mL,
$C_S(t)$ = radioactive concentration of tracer in the shunt compartment, nCi/mL,
$\dot{Q}_S$ = portion of regional blood flow to the shunt compartment, mL/sec, and
$\lambda_S \equiv \frac{C_{VB,S}}{C_S}$ = partition coefficient between non-aerated lung tissue and blood for $^{13}N_2$.

For this compartment, λ_S relates the tracer concentration in pulmonary venous blood $C_{VB,S}(t)$ leaving non-aerated alveolar units to the tissue and intraalveolar tracer concentration on these non-aerated units $C_S(t)$. The solubility of $^{13}N_2$ gas in blood, edema fluid and lung tissue (atelectatic alveoli, etc.) is assumed to be equal and thus $\lambda_S \approx 1$.

Analogous to equation (3), equation (7) was rewritten for tracer content in the compartment, given by the product of V_S and $C_S(t)$. Moving V_S inside the derivative on the left of equation (7) and rewriting $\dot{Q}_S$ in terms of $\dot{Q}_R$ and $\dot{Q}_T$ yields:

$$\frac{d}{dt}[V_S C_S(t)] = \dot{Q}_T \left(\frac{\dot{Q}_R}{\dot{Q}_T} \right) \left(\frac{\dot{Q}_S}{\dot{Q}_R} \right) C_{PA}(t) - \frac{[V_S C_S(t)]}{\tau_S} \tag{8}$$

where $\tau_S = \frac{V_S}{\dot{Q}_S}$ since we assume $\lambda_S \approx 1$. The inverse of τ_S is the transport rate constant for the compartment. The additional parameter to be identified from equation (8) is: τ_S.

2.1.5. Dual-Compartment Ventilation Model for Aerated Compartments

Equation (3) defines an aerated compartment with single compartment washout behavior. Tracer kinetics during the washout of normal lungs data is generally well characterized by a single exponential concentration function. Occasionally, as in lung regions partially filled with a perfluorocarbon liquid or regions with severely obstructed airways, slow washout rates are observed near the end of the imaging sequence. A dual-compartment ventilation model was introduced to account for this heterogeneous behavior. The model assumes that the aerated compartment of an ROI is further subdivided into two areas that ventilate at different rates. The fraction of blood flow to the aerated compartment is also subdivided between the two ventilating areas. Labeling the compartments as "fast" (1) and "slow" (2) and applying conservation of mass to the two control volumes provides the differential equations.

$$V_1 \frac{dC_1(t)}{dt} = \dot{Q}_1 C_{PA}(t) - \dot{Q}_1 \lambda_A C_1(t) - \dot{V}_1 C_1(t)$$
$$V_2 \frac{dC_2(t)}{dt} = \dot{Q}_2 C_{PA}(t) - \dot{Q}_2 \lambda_A C_2(t) - \dot{V}_2 C_2(t) \quad (9)$$

where

V_1 and V_2 = subcompartment volumes of distribution in the aerated compartment of the ROI, mL,

$C_1(t)$ and $C_2(t)$ = radioactive concentration functions of tracer in the aerated subcompartments, nCi/mL,

$\dot{Q}_1$ and $\dot{Q}_2$ = portions of aerated blood flow to the aerated subcompartments, mL/sec, and

$\dot{V}_1$ and $\dot{V}_2$ = subcompartment ventilation flow rates, mL/sec.

To rewrite equations (9) for tracer contents in the compartments given by the products $V_1C_1(t)$ and $V_2C_2(t)$, V_1 and V_2 are moved inside their respective derivatives on the left of the equations. By the same argument used for the modeling simplification in the single exponential washout model, we assume that $\left(\frac{\dot{Q}\lambda_A}{V}\right)_{1,2}$ are much longer than the apneic imaging period and thus the rate constant during apnea $\left(\frac{V}{\dot{Q}\lambda_A}\right)_{1,2}$ is approximately zero. Therefore, in each subcompartment, the tracer content remains virtually constant during apnea. Regional blood flow to the aerated compartment is distributed to the two ventilating areas, providing the continuity relationship: $\dot{Q}_A = \dot{Q}_1 + \dot{Q}_2$. Substituting this relationship into equations (9) and rewriting the blood flows $\dot{Q}_1$ and $\dot{Q}_2$ in terms of $\dot{Q}_R$, $\dot{Q}_S$ and $\dot{Q}_T$ yields:

$$\frac{d}{dt}[V_1 C_1(t)] = \dot{Q}_T \left(\frac{\dot{Q}_R}{\dot{Q}_T}\right)\left(1-\frac{\dot{Q}_S}{\dot{Q}_R}\right)\left(\frac{\dot{Q}_1}{\dot{Q}_A}\right) C_{PA}(t) - \left(s\dot{V}_{A,1}\right)[V_1 C_1(t)]$$

$$\frac{d}{dt}[V_2 C_2(t)] = Q_T \left(\frac{\dot{Q}_R}{\dot{Q}_T}\right)\left(1-\frac{\dot{Q}_S}{\dot{Q}_R}\right)\left(1-\frac{\dot{Q}_1}{\dot{Q}_A}\right) C_{PA}(t) - \left(s\dot{V}_{A,2}\right)[V_2 C_2(t)] \quad (10)$$

These equations introduce three additional parameters to be identified: $s\dot{V}_{A,1}$, $s\dot{V}_{A,2}$ and $\frac{\dot{Q}_1}{\dot{Q}_A}$. $s\dot{V}_{A,1}$ is the specific alveolar ventilation for the "fast" compartment. $s\dot{V}_{A,2}$ is the specific alveolar ventilation for the "slow" compartment. $\frac{\dot{Q}_1}{\dot{Q}_A}$ is the blood flow to the "fast" compartment expressed as a fraction of aerated compartment blood flow $\dot{Q}_A$. The fractional blood flow to the "slow" compartment is calculated from continuity: $\frac{\dot{Q}_2}{\dot{Q}_A} = 1 - \frac{\dot{Q}_1}{\dot{Q}_A}$.

2.1.6. Positron Emission Tomography (PET) Camera

The PET camera does not acquire instantaneous count rates. Rather, it accumulates radioactive decay events for a discrete interval equal to the imaging time period (Δt_{img}). The PET camera therefore effectively performs an integration of the sum of the tracer content functions described by the compartmental differential equations. The input signal to the camera is normalized by image collection time to yield average tracer activity in radioactive units per unit volume of thoracic tissue. A data point (S_i) corresponding to a ROI from an image collected between times t_i to ($t_i + \Delta t_{img}$) is:

$$S_i = \frac{1}{\Delta t_{img}} \int_{t_i}^{t_i + \Delta t_{img}} V_S C_S(t) + V_A C_A(t) \qquad (11)$$

for the single compartment washout model, or:

$$S_i = \frac{1}{\Delta t_{img}} \int_{t_i}^{t_i + \Delta t_{img}} V_S C_S(t) + V_1 C_1(t) + V_2 C_2(t) \qquad (12)$$

for the dual-compartment washout model.

2.1.7. Recirculation

In cases of lungs with large areas of shunt, we observed that during the last 30 seconds of apnea the concentration of tracer in the nondependent ROI increased (figure 2). We assumed that such an increase in concentration could be attributed to the arrival of tracer that had bypassed the non-aerated alveoli and recirculated back to the lung. In the top of figure (2), a positive slope in the nondependent ROI data was observed during the last half of the apneic tracer kinetics.

As the tracer bypasses the lung with shunted blood flow, it circulates through the systemic circulation (arterial and venous blood vessels), back to the right heart, and into the pulmonary circulation reaching the capillary-alveoli interface for a second time. In our studies, the tracer concentration of recirculating blood or the volume of blood through which the tracer was diluted, however, were unknown. To solve equation (2) with recirculation, two additional required parameters were C_R, the specific activity of recirculating blood, and $\Delta t_{rec.conc.}$, the time delay of recirculation. C_R multiplied by the total cardiac output $\dot{Q}_T$ is the recirculated activity per unit time. A recirculation fraction

is this product $\dot{Q}_T C_R$ normalized by the injected radioactivity per unit time (the product of $\dot{Q}_I$ and C_I). As a first order approximation, this recirculation fraction per unit time (F_R) was estimated from the slope of the nondependent apneic tracer kinetics data (normalized by the total injected infusate) in cases where shunt was present in the middle and dependent ROI's (figure 2, *bottom*).

$$F_R = \frac{\Delta Radioactivity}{\Delta t_{rec.conc.}} \tag{13}$$

where $\Delta Radioactivity$ is the change in radioactivity over the last half of the normalized nondependent tracer kinetics data and $\Delta t_{rec.conc.}$ is the time difference between these tracer kinetics data (i.e., 30 seconds for a 60-second apneic period). Increase in radioactivity above that given by equation (13) must be the effects of interregional mass diffusion, cardiogenic mixing between adjacent ROI's, or other phenomena not incorporated into the current model. Moreover, significant shunt in any of the three ROI's in healthy, normal animals is rare and the effects of recirculation are therefore neglected.

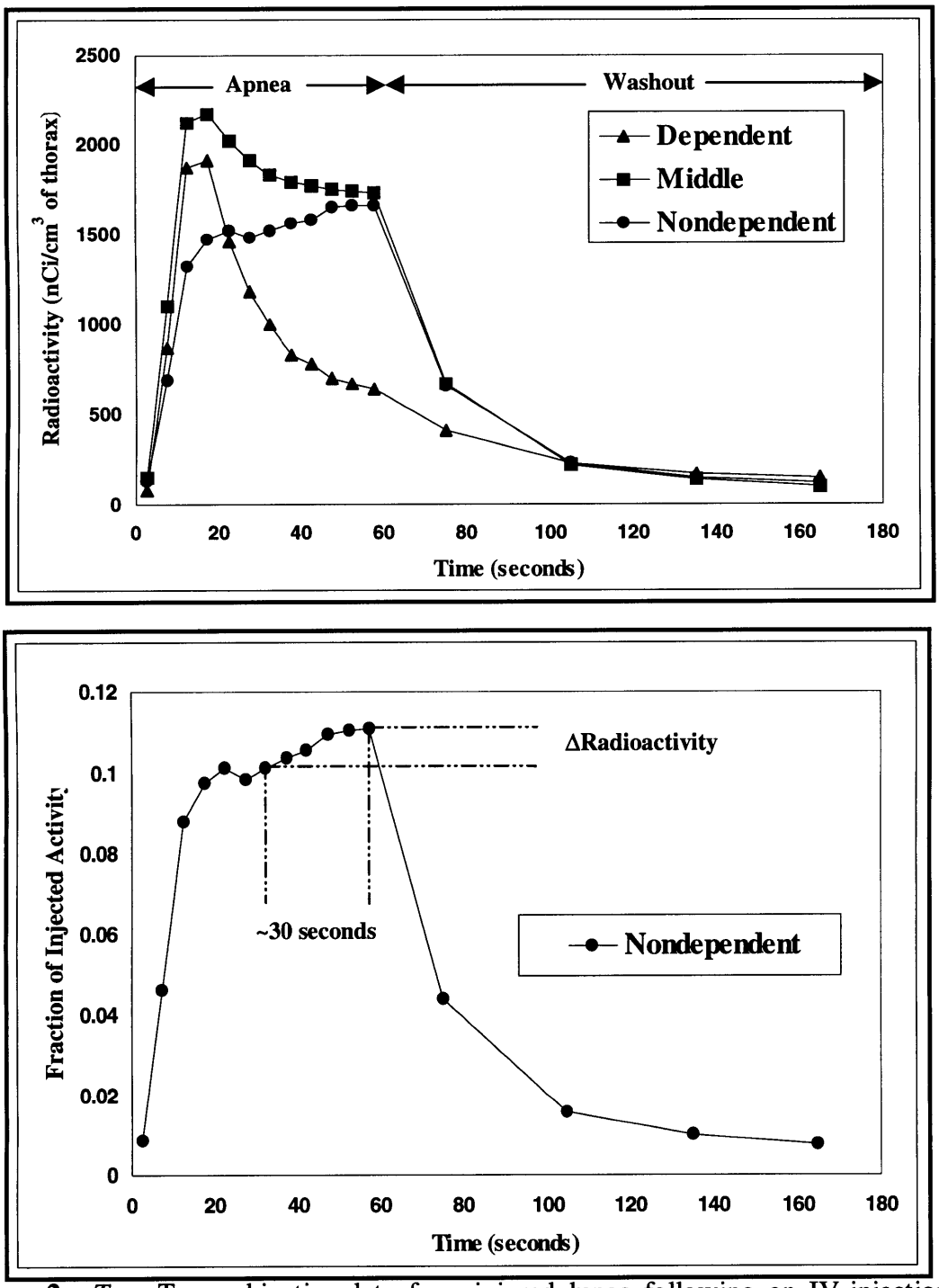

Figure 2. *Top*: Tracer kinetics data from injured lungs following an IV-injection of $^{13}N_2$-labeled saline. In the middle and dependent ROI's, tracer climbs towards a peak and then declines exponentially as $^{13}N_2$ is removed from atelectatic alveolar units by shunt blood flow. The gradual rise observed in the nondependent ROI beyond ~30 seconds rise may be partially accounted for by tracer recirculation given the significant shunt present in the middle and dependent ROI's. *Bottom*: Nondependent data expressed as a fraction of the total injected infusate. For the model, the recirculation fraction per unit time (F_R) was taken as Δ*Radioactivity*/30 seconds.

2.2. Nonlinear System Identification

To fit the differential equations developed in the previous section to PET data, nonlinear system identification techniques were utilized. System identification is the process of deriving the parameters of a system model from observed input and output signals. The goal is to find the parameter set $(p_1, p_2, \ldots, p_n)$ of a model described by its differential equations such that its output $M(t_i)$ matches the output of a real system $S(t_i)$ sampled at discrete times $(t_1, t_2, \ldots, t_n)$. The quality of fit is measured using a global error calculation. A gradient-descent search algorithm is implemented that attempts to minimize a multidimensional cost function, which ordinarily is defined as the sum-of-squared errors between the model output and the experimental data.

$$E(p_1, p_2, \ldots, p_n) = \sum_{i=1}^{n} \left[M(t_i) - S(t_i) \right]^2 \tag{14}$$

Since the model was nonlinear, it was not practical to compute derivatives $\frac{\partial E}{\partial p_1}, \frac{\partial E}{\partial p_2}, \ldots, \frac{\partial E}{\partial p_n}$, set them equal to zero, and solve for the parameter set $(p_1, p_2, \ldots, p_n)$ because the resulting equations would also be nonlinear and typically without an analytical solution. Nonlinear system identification is forced to resort to numerical minimization algorithms (e.g., Gauss-Newton, Levenberg-Marquardt) to find the optimal parameter set $(p_1, p_2, \ldots, p_n)$ for minimal $E(p_1, p_2, \ldots, p_n)$.

The gradient of a multidimensional scalar function is a vector denoted "∇" and mathematically given by $\nabla E = \frac{\partial E}{\partial p_1}\vec{p}_1 + \frac{\partial E}{\partial p_2}\vec{p}_2 + \ldots + \frac{\partial E}{\partial p_n}\vec{p}_n$, where $(\vec{p}_1, \vec{p}_2, \ldots, \vec{p}_n)$ are unit vectors along the axes of $E(p_1, p_2, \ldots, p_n)$ defined by the parameters $(p_1, p_2, \ldots, p_n)$. The

gradient vector is normal to the surface of $E(p_1, p_2, \ldots p_n)$ at every point and its projection is in the direction in which $E(p_1, p_2, \ldots p_n)$ undergoes the greatest rate of increase. Since the goal is to minimize $E(p_1, p_2, \ldots, p_n)$, the inverse (i.e., negative) of ∇E provides the next feasible search direction relative to the error function surface for the gradient-descent search algorithm at the current parameter set $(p_1, p_2, \ldots, p_n)$. Thus, an iterative procedure is established.

The differential equations of the model were formulated and solved using Matlab's numerical integration toolbox SIMULINK (The MathWorks, Nattick, MA) and specialized software designed to optimize nonlinear error functions with identified parameter vectors.

A bolus of $^{13}N_2$-labeled saline in our imaging protocol is the physiologic system input. For the SIMULINK model, this input signal was taken as an ideal square pulse with its height equal to the infusion flow rate $\dot{Q}_I$ = 3.33 mL/sec for the time duration of t_{bolus} seconds. The area beneath this square pulse ($\dot{Q}_I t_{bolus}$) multiplied by the infusate specific activity (C_I) is the total injected radioactivity. Recirculation was also simulated as a square pulse with its flow rate equal to $\dot{Q}_T$. The signal starts at t_{start} = 30 seconds, since this was consistently the observed onset of increased activity in the nondependent data. The signal was ended with apnea plus t_{start} (i.e., $t_{finish} = 60 + t_{start} = 90$ seconds) for the following reason. If there is recirculation of activity, its specific activity in blood should be continuously diluted with each passage through the systemic and pulmonary circulation. By ending the recirculation signal at 90 seconds, we have assumed that when the recirculated activity reached the lung for the third time, its effect was negligible.

Thus, the term $\dot{Q}_T C_R$ on the right of equation (2) was assumed to be negligible relative to the other terms in the equation. The height of the pulse is the recirculation fraction per unit time F_R given by equation (13). The area beneath the pulse is therefore the total recirculated activity expressed as a fraction of the total infused radioactivity.

The solutions to the compartment differential equations for times defined by $t < \Delta t_{TD}$ are trivially zero, and greater than zero for $t > \Delta t_{TD}$. The same time-shifted input signal $C_{PA}(t)$ is input to both ROI compartments for a time duration equal to the period of apnea used in the original image collection. After the simulation of the apneic period, a step-input signal is introduced into the aerated compartment of the ROI to simulate tracer removal by ventilation. The height of the step input is equal to the specific alveolar ventilation for the region. In the SIMULINK model, the PET camera integrates the sum of the compartmental activities for the full simulation period (apnea plus washout). The PET camera output must therefore be sampled at discrete points and normalized by image collection time to yield the equivalent of an imaging data point. We used Euler's numerical integration scheme with an incremental time stepping of 0.1 seconds. The simulation time was 180 seconds, the time of the perfusion-washout image protocol (60 seconds of apnea plus 120 seconds of washout). The PET camera input from SIMULINK was a discrete array of 1801 points, and the discrete output of the PET camera model $M(t_i)$ was thus:

$$M(t_1, t_2, \ldots, t_n) = \frac{1}{\Delta t_{img,1}} \int_0^{\Delta t_{img,1}} V_S C_S(t) + V_A C_A(t) dt,$$
$$\frac{1}{\Delta t_{img,2}} \int_{\Delta t_{img,1}}^{\Delta t_{img,2}} V_S C_S(t) + V_A C_A(t) dt, \ldots, \frac{1}{\Delta t_{img,n}} \int_{\Delta t_{img,n-1}}^{\Delta t_{img,n}} V_S C_S(t) + V_A C_A(t) dt \quad (15)$$

where n is the number of PET images collected in the sequence. For the dual-compartment ventilation model, the integrands in equation (15) are replaced by $V_S C_S(t) + V_1 C_1(t) + V_2 C_2(t)$. Equation (15) defines an array of n data points used in equation (14) to calculate the sum-of-squared errors.

We performed a nonlinear system identification (error function optimization) with a home-adaptation of a specialized software package designed for compatibility with SIMULINK models. Control system engineers at Cambridge Control Ltd. (Cambridge, UK) originally developed a Nonlinear Identification Toolkit (NLID) [1]. It allows variable parameters in the SIMULINK model built from the state-space representation of the governing differential equations. Since the PET system identification problem presents the additional caveat that the model output is the integral over a specified imaging interval of the differential equation solutions, it was necessary to modify the error function calculation in the code of NLID. Also, since the model is nonlinear, the parameters obtained may have multiple local minima. NLID is thus equipped with the option to perturb automatically and radically initial parameter guesses (within parameter bounds) for maximal error function coverage and approximation to a true global minimum.

2.2.1. Parameter Identification Methodology

The time necessary for nonlinear optimization grows exponentially with the number of parameters to be identified. Given the limited number of imaging data points provided by PET, and the number of parameters of the model, we developed a strategy of system identification to minimize the search time.

Imaging data was normalized by the total injected radioactivity for parameter identification. Total injected radioactivity is equal to the product of the infusion volume flow rate $\dot{Q}_I$, bolus injection time t_{bolus} and infusate specific activity C_I. The idealized $^{13}N_2$-labeled saline square pulse therefore injects 1 unit of normalized radioactivity over the injection time t_{bolus}. The height of the pulse was thus adjusted to be $\frac{1}{t_{bolus}}$.

During a typical PET study, the imaging sequence consisted of two phases: a period of apnea, during which perfusion data was collected, followed by ventilation, during which washout data was collected. The differential equations are decoupled with respect to these two imaging phases, since ventilation simulation starts at the end of apnea. It was therefore possible to identify the parameters associated with each data set separately. The perfusion and shunt parameters were identified first from the apneic imaging data, and the ventilation parameters second from the washout imaging data running the model with the previously identified perfusion parameters. One ROI was identified at a time.

Parameters from the nondependent ROI were identified first. Tracer kinetics data in this region typically show no drop in activity during apnea and were therefore modeled entirely by equations (2) and (3), or (2) and (9) if the dual-compartment washout model was required. If a positive slope was observed over the last 30 seconds of apnea, equation (13) was used to calculate the recirculation fraction per unit time F_R. Two parameters were identified from the nondependent tracer kinetics data: the regional perfusion fraction ($\frac{\dot{Q}_R}{\dot{Q}_T}$) and mean tracer transit time Δt_{TD}.

Infrequently, however, tracer kinetics data showed drops in activity in all ROI's (figure 3). In those cases, F_R could not be calculated. The data had to be modeled with the two-compartment model. Three parameters were identified with data showing a drop in regional activity during apnea: the regional perfusion fraction ($\frac{\dot{Q}_R}{\dot{Q}_T}$), the shunt fraction ($\frac{\dot{Q}_S}{\dot{Q}_R}$) and the time constant associated with the shunt compartment (τ_S). Once these were identified, they are fixed in the model and used to identify the parameters related to the tracer washout: specific alveolar ventilation ($s\dot{V}_A$) for the single compartment model, or $s\dot{V}_{A,1}$, $s\dot{V}_{A,2}$ and $\frac{\dot{Q}_1}{\dot{Q}_A}$ for the dual-compartment model.

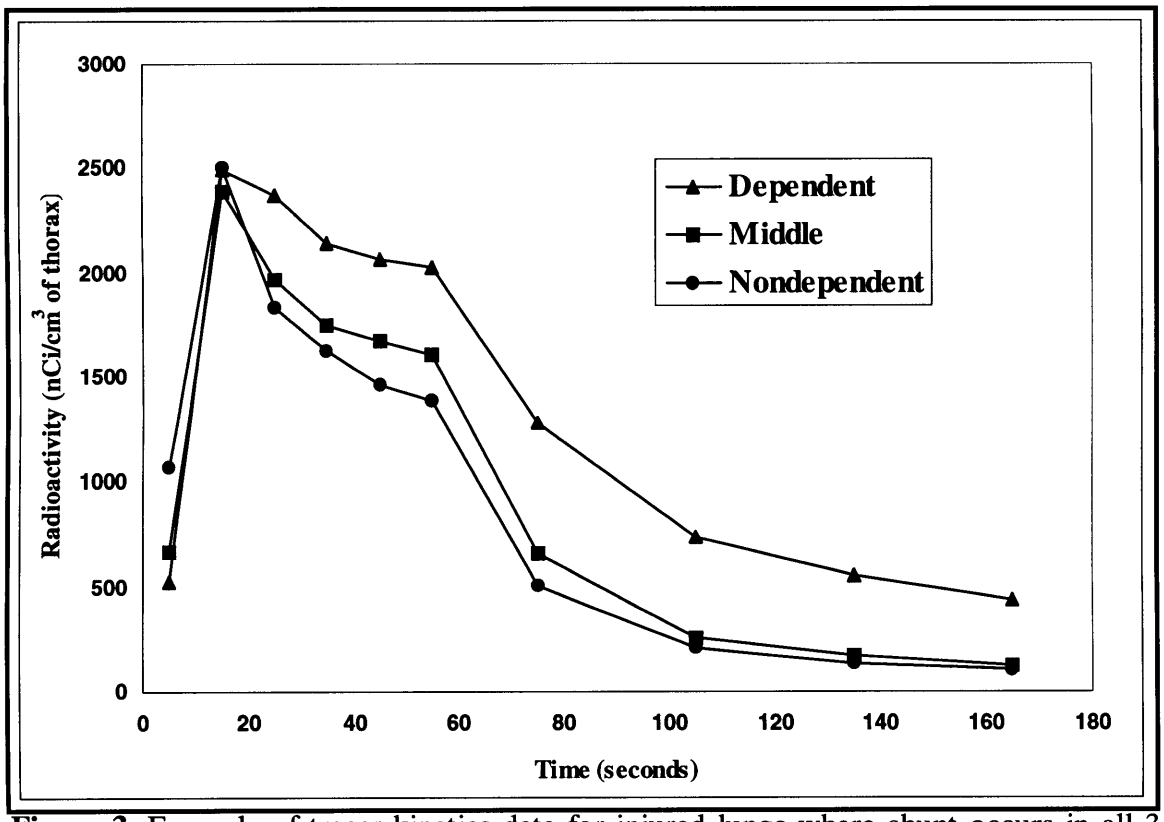

Figure 3. Example of tracer kinetics data for injured lungs where shunt occurs in all 3 ROI's. $^{13}N_2$ reaches a peak value in all 3 ROI's and then declines exponentially as it is removed from he imaging region by reabsorbtion into shunt blood flow. The recirculation fraction per unit time F_R is not accessible with the current model since a rise in activity for $t > 30$ seconds is not observed in the nondependent ROI.

2.2.2. Parameter Bounds and Initial Estimates

- **Mixing Volume (V_H) and Tracer Transit Time (Δt_{TD})**

Selection of an appropriate V_H and Δt_{TD} was based on the best fit of the model to the data from the first two PET images (the data affected by the parameters). The first image is affected primarily by the tracer arrival time, and principally the mixing volume affects the second image. Adequate fit of the model to the first two data points ensured appropriate identification of the parameters associated with the rest of the data. We used a fixed mixing blood volume of 50 mL (the estimated volume of the right heart plus a

fraction of the pulmonary arterial tree for our experimental animals) and adjusted transit time delay yielding values on the order of 3 seconds or less.

- **Perfusion Related Parameters**

An initial estimate of $\frac{\dot{Q}_R}{\dot{Q}_T}$ was visually obtained from the data normalized by the total injected radioactivity. For normal aerated lungs, the normalized data reached a plateau at a level proportional to $\frac{\dot{Q}_R}{\dot{Q}_T}$ because $^{13}N_2$ gas diffused into the alveolar airspace and approximately remained there for apneic imaging. This plateau level provided a good initial estimate of the parameter to be identified. In atelectatic regions, regional $^{13}N_2$ content reached a peak and declined towards an asymptote. An initial estimate of $\frac{\dot{Q}_S}{\dot{Q}_R}$ was given by: $1-\frac{C_F}{C_P}$, where C_P and C_F are the peak and final apneic data points, respectively. Fitting an exponential to the apneic regional tracer content data between the peak (C_P) and final (C_F) values yielded an initial estimate of τ_S. The initial guess was thus given by: $\tau_S = \frac{-\Delta t_{PF}}{\ln\left(\frac{C_F}{C_P}\right)}$, where Δt_{PF} is the time lapse between the initiation of collection of the corresponding PET images.

For middle and dependent ROI's, the tracer transport delay (Δt_{TD}) identified from the nondependent ROI was used as an initial estimate. After an initial identification of $\frac{\dot{Q}_R}{\dot{Q}_T}, \frac{\dot{Q}_S}{\dot{Q}_R}$, and τ_S using this initial estimate of Δt_{TD}, the model was simulated and Δt_{TD}

re-identified until the first data point of the model coincided exactly with the PET data.

$\frac{\dot{Q}_R}{\dot{Q}_T}, \frac{\dot{Q}_S}{\dot{Q}_R}$, and τ_S were then re-identified using the new Δt_{TD}.

- **Washout Related Parameters**

In the absence of the evidence of regional shunt behavior (no loss of regional activity during apnea), initial estimates of an ROI's $s\dot{V}_A$ were obtained by finding the exponential function that described the first (C_1) and last (C_4) data points of the washouts. The initial guess was calculated with: $\tau_{WO} = \frac{-\Delta t_{14}}{\ln\left(\frac{C_4}{C_1}\right)}$, where Δt_{14} is the time lapse between the initiation of collection of the corresponding PET images. For a monoexponential washout, the inverse of the washout time constant is the specific alveolar ventilation [11]. Thus, $\frac{1}{\tau_{WO}}$ was used as an initial guess for $s\dot{V}_A$.

In ROI's with tracer content loss during apnea, initial guesses and parameter bounds were defined in the following manner. First, the ROI's tracer content was corrected for contributions of tracer present in the shunt compartment as predicted with the model simulation. Using the parameters identified from the apneic data ($\Delta t_{TD}, \frac{\dot{Q}_R}{\dot{Q}_T}, \frac{\dot{Q}_S}{\dot{Q}_R}$, and τ_S), the model was simulated for the shunt compartment tracer content. The simulated data points of shunt compartment tracer content during the washout were subtracted from the corresponding experimental PET data to give an estimate of tracer content in the non-shunting units during the washout. A single

exponential was then fitted to the first two "shunt-corrected" tracer content data from the washout (C_1, C_2) to give an initial estimate of the time constant for the fast-ventilated subcompartment: $\tau_{FAST} = -\frac{\Delta t_{12}}{\ln\left(\frac{C_2}{C_1}\right)}$, where Δt_{12} is the time lapse between the initiation of the collection of the first and second PET images of the washout. The true τ_{FAST} cannot be longer than this estimate since the calculation does not exclude activity from the slow compartment. Since $s\dot{V}_{A,FAST} = \frac{1}{\tau_{FAST}}$, the minimum $s\dot{V}_{A,FAST}$ is $\frac{1}{\tau_{FAST}}$. An upper parameter bound for $s\dot{V}_{A,FAST}$ was established with approximate knowledge of the tidal volume (V_T), anatomic dead space (V_D), lung volume at functional residual capacity (V_{FRC}) and the breathing frequency (f_b) as $s\dot{V}_{A,FAST} \sim \frac{(V_T - V_D)}{V_{FRC}} f_b$. A typical V_{FRC} for our animals is about 500 mL. If one assumes $V_T \sim 300$ mL, neglects the dead space and uses f_b of 10 breaths/min, then the maximum $s\dot{V}_{A,FAST}$ is ~ 0.36 sec^{-1}. We set the maximum $s\dot{V}_{A,FAST}$ at 1 sec^{-1}.

A second single exponential was defined from the last two "shunt-corrected" aerated tracer content data points from the washout (C_3, C_4) yielding: $\tau_{SLOW} = -\frac{\Delta t_{34}}{\ln\left(\frac{C_4}{C_3}\right)}$, where Δt_{34} is the time lapse between the initiation of collection of the third and fourth PET washout images. The true τ_{SLOW} cannot be shorter than this estimate since the calculation may still include activity from fast compartment. The longest τ_{SLOW} could be

infinity. Since $s\dot{V}_{A,SLOW} = \frac{1}{\tau_{SLOW}}$, the minimum $s\dot{V}_{A,SLOW}$ was taken as zero and the maximum $s\dot{V}_{A,SLOW}$ as $\frac{1}{\tau_{SLOW}}$.

2.3. Test of the Model with Experimental PET Images

The model was tested with experimental PET images from surfactant depleted lungs before and after partial liquid ventilation (PLV). Images were analyzed for averaged tracer kinetics data in three regions of interest along their vertical axis: dependent, middle and nondependent. The model was then fitted to the tracer kinetics data to identify the following regional parameters: $\Delta t_{TD}, \frac{\dot{Q}_R}{\dot{Q}_T}, \frac{\dot{Q}_S}{\dot{Q}_R}, \tau_S$, and $s\dot{V}_A$.

2.3.1. Animal Preparation

The Massachusetts General Hospital (MGH) Committee on Animal Care approved the experimental protocol for these animal experiments.

Sheep (~10 to 18kg) were intubated with a 7.5mm ID endotracheal tube and mechanically ventilated under general anesthesia (sodium pentothal). The ventilator was set at a breathing frequency of 10 breaths/minute and with an inspiratory time of 30% of the breathing period. Tidal volume was initially based on the weight of the animal and adjusted to maintain stable normocapnic arterial blood gases (45mmHg > P_aCO_2 > 35mmHg). Positive end expiratory pressure (PEEP) was maintained at 5cm H_20. The right femoral artery was cannulated for monitoring pressure and arterial blood gases. A continuous infusion of anesthetic was administered through a catheter in the right femoral vein. A Swan-Ganz catheter was inserted in the left femoral vein and advanced into the pulmonary artery for sampling of mixed venous blood gases, and measurements of

pulmonary artery pressure and total cardiac output ($\dot{Q}_T$). An additional catheter was placed in the right external jugular vein for administration of $^{13}N_2$-labeled saline. Tween-80 saline was used to induce a bilateral lavage.

2.3.2. Experimental Apparatus

The experimental apparatus included a multiple-ring PET camera, a mechanical ventilator and a saline labeling system. The multiple-ring PET camera at the MGH used was capable of imaging three-dimensional sections of the thorax (greater than 70% of the lung) with a maximum spatial resolution of 7 mm. A three-dimensional image consisted of 15 planar slices with thickness 6 mm and voxel size of 2 × 2 mm. An unimaged distance of ½ mm separates each slice.

CO_2 gas carried $^{13}N_2$ in trace amounts delivered by a cyclotron to the saline labeling system. This system separated the $^{13}N_2$ molecules from the CO_2 and ultimately dissolved them in previously degassed saline. A total volume of 200 mL of $^{13}N_2$-labeled saline was produced and temporarily stored in a pressurized chamber (~50psi) for subsequent intravenous infusion into the animal via the cannulated external jugular vein. The infusion system includes a remotely controlled valve system that allows flushing with $^{13}N_2$-labeled saline of the tubes between the storing chamber and the infusion catheter in the animal. $^{13}N_2$-labeled saline is delivered as a rapid bolus at an infusion flow rate ($\dot{Q}_I$) of 3.33 mL/sec.

2.3.3. Image Protocols

2.3.3.1. Positioning the Lung Field in the PET Camera

Animals lied supine in a plastic hemi-cylinder that is advanced into the field of view of the PET camera to cover an imaged distance of 9.75cm. The imaged lung section

ranges from a cross-section intersecting the heart to a cross-section intersecting the diaphragm. Confirmation of the imaged section was achieved by reconstructing a short duration (~10 minutes) positioning scan, collected by orbiting a radioactive pin concentric to the circular array of detectors and the animal's thoracic cage.

2.3.3.2. Rapid Intravenous Bolus Injection during Apnea: Perfusion and Washout

Sheep were imaged ~ 90 minutes after the bilateral lavage and ~ 30 minutes after the subsequent intratracheal instillation of LiquiVent™.

Mechanical ventilation was interrupted at functional residual capacity and immediately a bolus of $^{13}N_2$-labeled saline was infused through an external jugular vein cannula. Simultaneously with the beginning of infusion, collection of a sequence of consecutive PET images was initiated for the duration of apnea (60 seconds). Image collection time was 10 seconds giving 6 images for 3 animals, and 5 seconds giving 12 images for 2 animals. After this period of apnea, mechanical ventilation was restarted and an additional sequence of 4 images (each image 30 seconds in duration) was collected. The animal's cardiac output ($\dot{Q}_T$) was recorded just prior to imaging and a sample of the infusate was collected to assess its specific activity (C_I).

2.3.3.3. Transmission and Uniformity Scans

Transmission scans were collected and used in the image reconstruction process to correct the local data for energy attenuation caused by body tissues, liquid respiratory media, and PET camera supporting structures. Uniformity scans were collected before and after the experiment, with nothing in the imaging field. Uniformity scans were used in the sinogram reconstruction process to correct for nonuniform detector sensitivity.

2.3.4. PET Image Analysis: Regional Tracer Kinetics Data

Collected sinograms were reconstructed into three-dimensional images using a convolution-back projection algorithm (effective spatial resolution of 7 mm). Reconstructed images, in units of nCi/cm^3 of thoracic tissue, were used to calculate regional tracer kinetics data as follows.

A unity mask was created covering the imaged lung field to exclude voxels in extrapulmonary regions. Masks were manually delineated, slice-by-slice, from either the corresponding reconstructed transmission scan or from the sum of all perfusion images taken after arrival of the tracer to the alveolar spaces. The unity mask was multiplied voxel-by-voxel to the first perfusion image, and the result was used to highlight and remove from the mask areas corresponding to the injection catheter or the heart that inadvertently may have been included.

Three regions of interest (ROI) were defined from the refined mask along the vertical axis: nondependent, middle and dependent. To create the ROI's, the first uppermost and lowermost rows with nonzero voxel values of the three-dimensional mask were determined and the mask was divided into three ROI's of equal height. The volume of each ROI was calculated from the corresponding number of voxels. ROI volumes were typically 25%, 50% and 25% of the voxels in the full lung mask for the nondependent, middle and dependent regions, respectively.

Average specific activity in each ROI was then calculated for each sequential PET image. The resulting tracer kinetics data were decay-corrected to a reference time taken as the onset of intravenous injection. If $A(t)$ represents the instantaneous activity of the gas at time t and A_o is its initial activity, then radioactive decay obeys the equation:

$A(t) = A_o e^{-\frac{t}{\tau_{13_{N_2}}}}$, where $\tau_{13_{N_2}}$ is the radioisotope half-life $t_{1/2}$ (for $^{13}N_2$, $t_{1/2}$ ~ 9.96 minutes) divided by the natural logarithm of 2 (ln 2). An appropriate decay-correction factor for the tracer kinetics data takes into account the decay associated with the time difference between the start of the image collection and the onset of infusion (t_o) plus the decay associated with the time of image collection (Δt_{img}). Integrating $A(t) = A_o e^{-\frac{t}{\tau_{13_{N_2}}}}$ between t_o and ($t_o + \Delta t_{img}$) and normalizing by Δt_{img} provides the decay-correction factor (f_{DC}) used:

$$f_{DC} = \frac{\Delta t_{img} e^{\frac{t_o}{\tau_{13_{N_2}}}}}{\tau_{13_{N_2}} \left(1 - e^{-\frac{\Delta t_{img}}{\tau_{13_{N_2}}}}\right)}.$$

Infusate specific activities were measured in a radiation counter previously cross-calibrated with the PET camera. This activity was also corrected to the same reference time as the tracer kinetics data. Tracer kinetics data were then plotted versus time in seconds, with each data point plotted at the middle of the image collection time interval.

2.3.5. Post-Processing Derived Parameters

This section describes the post-processing of the parameters identified by fitting the model to the experimental PET data defined above. Parameters from each ROI were further normalized to yield the following parameters:

1. Average regional perfusion per voxel of an ROI relative to the average perfusion per voxel of the imaged lung field as:

$$\dot{Q}_{r_i} = \frac{\frac{\left(\frac{\dot{Q}_R}{\dot{Q}_T}\right)_i}{Vox_i}}{\frac{\sum_{i=1}^{3}\left(\frac{\dot{Q}_R}{\dot{Q}_T}\right)_i}{\sum_{i=1}^{3} Vox_i}} \tag{16}$$

where Vox_i is the number of voxels in the ROI and i is a subscript denoting the ROI (nondependent, middle or dependent).

2. Imaged lung shunt fraction. To estimate the fraction of shunt from the total blood flow to the imaged lung, we added the products of the regional shunt fractions multiplied by the regional perfusion fraction of all ROI's and normalized it by the total perfusion to the imaged section of the lung.

$$\frac{\sum \dot{Q}_S}{\sum \dot{Q}_R} = \frac{\sum_{i=1}^{3}\left[\left(\frac{\dot{Q}_R}{\dot{Q}_T}\right)\left(\frac{\dot{Q}_S}{\dot{Q}_R}\right)\right]_i}{\sum_{i=1}^{3}\left(\frac{\dot{Q}_R}{\dot{Q}_T}\right)_i} \tag{17}$$

3. Effective specific ventilation. For the single compartment model, the parameter identified was the regional $s\dot{V}_A$ of an ROI. For a dual-compartment model, an effective $s\dot{V}_A$ was calculated as a perfusion-weighted average of the $s\dot{V}_A$'s from each compartment:

$$s\dot{V}_A = \left(\frac{\dot{Q}_1}{\dot{Q}_A}\right) s\dot{V}_{A,1} + \left(\frac{\dot{Q}_2}{\dot{Q}_A}\right) s\dot{V}_{A,2} \tag{18}$$

The calculation of the perfusion-weighted $s\dot{V}_A$ required the assumption that the fractional subcompartment volumes of distribution are proportional to their respective fractions of aerated blood flow: $\frac{\dot{Q}_1}{\dot{Q}_2} \propto \frac{V_1}{V_A}$ and $\frac{\dot{Q}_2}{\dot{Q}_A} \propto \frac{V_2}{V_A}$. The basis of this assumption rests on the fact that the model simulated washout data is intrinsically weighted by the perfusion data.

3. RESULTS

The model fit the data well (figure 4). For lavage lungs, mean R^2's were 0.9945 ± 0.0030, 0.9996 ± 0.0002, and 0.9992 ± 0.0005 for the nondependent, middle and dependent ROI's, respectively. For the lungs under PLV, they were similar: 0.9966 ± 0.0014, 0.9996 ± 0.0003, and 0.9988 ± 0.0011 for the nondependent, middle and dependent ROI's, respectively. Results averaged for five sheep are presented in Table (1). The post-processed data averaged for the five sheep are presented in Table (2). An average shunt fraction was highest in the dependent region for the lavage lungs (0.7526 ± 0.1055), 0.4636 ± 0.1500 in the middle region and zero in the nondependent region. During PLV, the model identified considerably reduced shunt fractions of 0.4530 ± 0.0834 and 0.2953 ± 0.1895 in the dependent and middle regions, respectively. A nonzero shunt fraction of 0.1453 was identified in the nondependent region for one sheep. The loss of tracer during apnea occurred faster in the lavage lungs (τ_S = 10.5018 ± 3.2749 sec and 10.5006 ± 2.6500 sec for the middle and dependent ROI's, respectively)

than during PLV (τ_S = 26.1445 ± 10.9119 sec and 35.9702 ± 25.9227 sec for the middle and dependent ROI's, respectively). Specific ventilation for the lavage lungs was greatest in the middle regions (0.0983 ± 0.0282 sec^{-1}) and similar in the nondependent and middle regions (0.0692 ± 0.0218 sec^{-1} and 0.0638 ± 0.0374 sec^{-1}, respectively). Specific ventilation increased during PLV in the nondependent ROI to 0.0924 ± 0.0339 sec^{-1}, but decreased in the middle and dependent ROI's to 0.0743 ± 0.0124 sec^{-1} and 0.0153 ± 0.0041 sec^{-1}, respectively, demonstrating that regions of the lung filled with perfluorocarbon liquid were hypoventilated. The global index of shunt (imaged lung shunt fraction) was statistically larger for the lavage lungs (0.5265 ± 0.0789) than during PLV (0.3252 ± 0.1392), indicating that PLV reduced shunt in these surfactant deficient lungs.

4. DISCUSSION

The model represented a refinement of the methods described by Mijailovich et. al. [5], which was only valid for normal lungs. We developed a tracer kinetics model for quantitative analysis of PET following an apneic bolus injection of $^{13}N_2$-labeled saline that can be used in normal *and* injured lungs. Two important characteristics of the model are:

1. The model allows estimation of regional perfusion fractions ($\frac{\dot{Q}_R}{\dot{Q}_T}$) in areas of the lung with intrapulmonary shunt. In these areas, the tracer $^{13}N_2$ does not remain constant during apnea but is removed by back diffusion into the pulmonary circulation.

2. The model calculates regional specific alveolar ventilation ($s\dot{V}_A$) from the PET imaging washout data in diseased lungs in the presence of shunt. During washout imaging, alveolar tracer removal can occur by shunt in non-aerated alveolar units and ventilation in aerated alveolar units. If $s\dot{V}_A$ is quantified directly from tracer washout data, there is the possibility of its overestimation.

Two conclusions that reached after testing the model with the experimental PET data described in the previous sections are:

3. Partial liquid ventilation (PLV) reduces shunt blood flow in the surfactant deficient lung, possibly due to the reopening of atelectatic alveolar units.
4. A limitation of the developed model is its inability to differentiate mechanisms causing the loss of tracer during apneic imaging.

Advantages of the Model. The constant infusion (CI) technique documented by Rhodes et. al. [6][7] in 1989 demonstrated the feasibility of the non-invasive PET imaging methodology to collect data for the quantification of gas exchange variables. Mijailovich et. al. [5] made a modification to the CI technique to quantify gas exchange variables from the kinetics of $^{13}N_2$ following a single bolus injection of $^{13}N_2$-labeled saline during apnea. Given the high insolubility of $^{13}N_2$ gas, migration of the tracer from the pulmonary capillary vessels to the alveolar airspace is virtually guaranteed in the normal, gas ventilated lung. By assuming the $^{13}N_2$ gas remains approximately stationary in the lung during apneic imaging, local tracer is proportional to local perfusion. With the assumption, the mathematical methodologies offered by Mijailovich et. al. can be used to quantify regional pulmonary perfusion from the resulting functional images. Also, in the normal lung, the dominant mechanism of tracer removal from the imaging

region during the washout phase is ventilation. Thus, regional ventilation can be quantified directly from analysis of the PET images collected during the tracer washout.

In the diseased lung, applying the direct methods of Mijailovich et. al. [5] to PET images from the single apneic bolus injection technique has some limitations. The direct method of analysis to diseased lung PET data can underestimate regional perfusion from the apneic imaging data. Furthermore, the direct method does not offer a method to quantify fractions of regional shunt blood flow since its development was based primarily on the normal lung. Following the apneic bolus injection of $^{13}N_2$-labeled saline in the diseased lung, the loss of tracer during apnea may not be limited to its minimal reabsorbtion from alveolar airspace into blood and body tissue. Diffusion of the tracer into non-aerated alveoli from blood is not nearly as complete as its diffusion into airspace. Qualitatively, this is because the solubility of $^{13}N_2$ in non-aerated lung tissue (e.g., atelectatic or edematous alveoli) is not much different than its solubility in blood. Thus, reabsorbtion of the tracer into intrapulmonary shunt blood flow and its lack of diffusion into the atelectatic or edematous units can cause substantial removal of the tracer from the imaging region during apnea. Moreover, for injection times longer than the injection site-to-ROI tracer transit times, reabsorbtion of the tracer by shunt flow can occur simultaneously with the injection. Thus, given these possibilities for the diseased lung and the signal averaging performed by the PET instrumentation, the resulting apneic voxel tracer contents may not accurately reflect local perfusion. The direct method applied to the resulting PET images therefore cannot be used to accurately quantify regional perfusion. There is the possibility of regional perfusion underestimation since the underlying assumption of tracer remaining confined to the alveolar airspace during

apneic imaging is no longer valid. The shunt fraction may also be underestimated using the previously described method for its initial guess: $\frac{\dot{Q}_S}{\dot{Q}_R} \approx 1 - \frac{C_F}{C_P}$. This is because C_P itself may not reflect regional perfusion.

Quantifying regional specific ventilation directly from PET washout data in the diseased lung may overestimate regional specific ventilation. In the diseased lung, particularly those with large areas of shunt, the mechanisms of the removal of tracer from the imaging region during the washout may not be limited to ventilation. This depends on the time constant characterizing the loss of tracer during apnea (by virtue of shunt blood flow) relative to the duration of apnea. If this time constant is short such that apneic tracer removal from non-aerated alveolar units is completed prior to the ensuing washout, then the resulting plateau activity level should be proportional to regional blood flow to aerated lung tissue. Furthermore, it is possible to estimate the fraction of shunt blood flow by assessing the difference between the peak and final apneic activity levels: $\frac{\dot{Q}_S}{\dot{Q}_R} \approx 1 - \frac{C_F}{C_P}$. Washout data can then be used directly to quantify regional ventilation of the aerated alveolar units. However, if the time constant is long relative to the apneic period, then two competing mechanisms cause the removal of tracer during the washout phase: reabsorbtion of tracer by shunt blood flow bypassing non-aerated alveolar units and ventilation through the tracheobronchial tree from aerated alveolar units. Using the resultant washout data directly to quantify regional specific ventilation will therefore result in its overestimation because tracer washout is attributed entirely to ventilation.

We can support all of the preceding statements quantitatively with an example data set analyzed with the model. In the dependent ROI of the bilaterally lavaged lungs, the regional tracer kinetics data (normalized by the total amount of injected radioactivity) peaks at a level that would suggest a percentage of regional perfusion $\frac{\dot{Q}_R}{\dot{Q}_T}$ of about 15.5% (figure 5). By using $\frac{\dot{Q}_S}{\dot{Q}_R} = 1 - \frac{C_F}{C_P}$, the percentage of regional shunt blood flow $\frac{\dot{Q}_S}{\dot{Q}_R}$ is approximately 68%. After submitting this data set to the model, both parameters were identified to be larger: $\frac{\dot{Q}_R}{\dot{Q}_T}$ was identified as 23.79% and $\frac{\dot{Q}_S}{\dot{Q}_R}$ was identified as 81.07%. The simulated (instantaneous) tracer content curve $V_S C_S(t) + V_1 C_1(t) + V_2 C_2(t)$ of figure (5) appears to peak at about 16.5%. The reduction from ~16.5% to ~15.5% between the model simulated curve and the raw PET data can be attributed to the signal averaging of the PET camera. Finally, since the injection time is greater than the tracer arrival time (t_{bolus} = 10 seconds > Δt_{TD} = 2.25 seconds), removal of tracer by the shunt blood flow occurs simultaneously with the injection. Only with the model is $\frac{\dot{Q}_R}{\dot{Q}_T}$ of 23.79% identified. The constant-valued line in figure (5) is drawn at this level, and schematically shows the underestimation of regional perfusion from raw PET data in this dependent lung region with a large area of non-aerated alveoli. Beyond its peak value, the tracer content curve shows an exponential decline that essentially plateaus prior to the

ventilation simulation. The dominant mechanism of tracer removal during the washout is thus ventilation from the aerated spaces.

PLV Reduces Shunt in the Surfactant Deficient Lung. The conclusion reached after fitting the model to the regional tracer kinetics data from the lavage lungs was that the average imaged lung shunt fraction was statistically smaller during PLV (0.3252 ± 0.1392 during PLV versus 0.5265 ± 0.0789 for the lavage lungs). This suggests that PLV reduces shunt in the surfactant deficient lung. This data is consistent with our preliminary analyses of PET data [14] from oleic acid injured lungs, an animal model that includes the effects of increased microvascular permeability and impaired surfactant function. Preliminary analysis of this data showed that shunt decreased most notably in dependent lung regions during PLV, possibly due to the reopening of atelectatic alveoli. With a low dose of perflubron (9 cc/kg), shunt decreased by a factor of about 9 (averaged over 4 animals). With the high dose of perflubron (30 cc/kg), shunt decreased by a factor of about 4 (averaged over 3 dogs). In both studies, we concluded that regions of shunt were converted to regions of low $\dot{V}_A/\dot{Q}$, and that this was the basis for the observed improvement in oxygenation. For the oleic acid injured lungs with the low dose of perflubron, P_aO_2 increased from 62 to 78 Torr, and from 133 to 176 Torr with the high dose of perflubron. In the lavage lungs, P_aO_2 increased from 74 to 168 mm Hg during PLV. The conversion of shunt areas to low $\dot{V}_A/\dot{Q}$ areas was a result of the hypoventilation in liquid filled regions of the lung. In Table (1), for example, it is clear that $s\dot{V}_A$ decreased during PLV in the dependent ROI's of the lavage lungs by a factor of about 5. Given the high specific weight of the liquid and the influence of gravity,

intratracheally administered liquid will preferentially reside in dependent lung regions. The hypoventilation in these regions can thus be partially attributed to the following fact pointed out by West [15]: diffusion rates of gases through liquid barriers are many orders of magnitude slower than their diffusion rates through gas barriers. Finally, the decreased ventilation noted in liquid filled regions in both the oleic acid injured lungs and the surfactant depleted lungs is consistent with a statement made by Shaffer [10]. In his brief review of the literature, he notes that a persistent reported problem during liquid ventilation is CO_2 retention (hypercapnia) and subsequent acidosis that might be attributed to the hypoventilation of the liquid filled lung.

Interestingly, the results from the analysis of the PET lavage data contradict a currently reported finding [2] that PLV redistributes pulmonary blood flow away from dependent lung regions. Clearly from table (2), dependent relative regional perfusion did not substantially decrease during PLV. It was 1.1689 ± 0.1306 for the lavage lungs and 1.0882 ± 0.1493 during PLV. Considerable controversy [2][3][14][16][18] exists regarding the local regulatory mechanisms governing observed shifts in perfusion away from dependent lung regions during PLV in normal and injured lungs. One hypothesis claims that the high specific weight of the liquid compresses the pulmonary capillaries, thereby increasing blood flow resistance and preferentially redistributing flow to least-resistant middle and nondependent regions. It is theorized that this shift in blood flow is the mechanism responsible for improved $\dot{V}_A/\dot{Q}$ matching during PLV and therefore improved oxygenation.

The discrepancy in the lavage data analyzed with the model versus the data reported in [2] suggests that localized regulatory mechanisms other than the high specific

weight of the liquid could be responsible for shifts in perfusion away from dependent lung regions during PLV. We therefore theorized that during PLV in the normal lung, dependent lung regions would experience increased hypoxic pulmonary vasoconstriction (HPV). This HPV was thus believed to be the mechanism shifting perfusion. Preliminary analyses of data from another experimental PET study [3], which used combinations of inhaled and intravenous vasodilation in the normal lung during PLV, suggested that shifts in perfusion may be the additive effects of two mechanisms: high specific weight of the liquid and HPV. With the intravenous vasodilation, the shift in perfusion away from dependent lung regions with PLV was partially reversed. Thus, we concluded that in the normal lung the shift in perfusion was in part due to locally increased HPV. These conclusions from the vasodilation study suggest that in the lavage data the maintained dependent relative regional perfusion during PLV may be partially accounted for by the reopening of atelectatic alveoli and thus a reduction in HPV.

Model Limitations. The ability of the model to fit tracer kinetics data is limited under certain conditions. One noteworthy limitation is its inability to differentiate different mechanisms causing the loss of tracer from the imaged lung during apnea. During gas ventilation, we assumed no removal of tracer from the imaging region during apnea. This was the assumption of a rate constant $(\frac{1}{\tau_A})$ of zero in equation (4) for the aerated compartment of the model. The basis of this assumption is a result of the already mentioned low partition coefficient for $^{13}N_2$ between air and blood (1.8%). Thus, blood flowing from air-filled alveoli carries minimal tracer away with it, rendering the outflow term $\dot{Q}_A \lambda_A C_A(t)$ in equation (3) negligible relative to the other terms. We can therefore

expect that during gas ventilation the dominant mechanism of tracer loss from the imaging region during apnea is shunt blood flow. During PLV, however, we recognized that the assumption of a transport rate constant of zero in aerated compartment can result in model simulated data that poorly fits the PET data. Model identified parameters may therefore be erroneous and inconsistent with other global physiologic data. The partition coefficient between perflubron and blood is greater than the partition coefficient between air and blood. Qualitatively, this means pulmonary venous blood flowing from liquid-filled alveoli may carry substantial amounts of $^{13}N_2$ away with it, rendering the outflow term $\dot{Q}_A \lambda_A C_A(t)$ in equation (3) non-negligible relative to the other terms. Reabsorbtion of tracer by blood flowing from liquid-filled alveoli and the lack of tracer diffusion from blood to liquid-filled alveoli can both be mechanisms responsible for the loss of tracer during apnea. Given our modeling simplification of $\frac{1}{\tau_A} \approx 0$ in the aerated compartment, however, the model attempts to fit the data by attributing all reduction in activity during the apneic simulation to the shunt blood flow. Hence, the identified shunt fraction may overestimate the true regional shunt.

We can demonstrate the breakdown of the assumption of $\frac{1}{\tau_A} \approx 0$ in the aerated compartment during PLV quantitatively with an example. In the middle ROI tracer kinetics data of one particular sheep during PLV, we observed that the loss of tracer during apnea was characterized by an unusually long time constant. The model was initially fitted to this data using the typical assumption of $\frac{1}{\tau_A} \approx 0$, and the following

physiological parameters were acquired: regional perfusion percentage $\frac{\dot{Q}_R}{\dot{Q}_T} = 46.58\%$, shunt blood flow percentage $\frac{\dot{Q}_S}{\dot{Q}_R} = 52.50\%$ time constant τ_S = 170.10 seconds, and specific alveolar ventilation $s\dot{V}_A$ = 0.1989 sec^{-1}. The resultant model fit to the PET data yielded an R^2 of 0.9859. Clearly, the model-simulated data does not fit the PET data during the washout phase (figure 6, *top*). The PET data shows washout of the regional activity, whereas the model grossly underestimates the regional $s\dot{V}_A$. It is not inconceivable that this poor fit is partially the fault of the zero rate constant assumption in the aerated compartment of the model. More than 50% of the regional blood flow is distributed to the shunt compartment that, in accordance with equation (7), does not ventilate and therefore remains during the washout. The identified time constant τ_S of 170.10 seconds requires a shunt compartment volume of distribution V_S of 1615.95 mL, whereas the volume of this middle ROI (V_{ROI}) is 270.50 mL. Since V_S is approximately 6 times larger than V_{ROI}, the tracer removal during apnea cannot possibly be purely the effects of shunt blood flow. To investigate this, we modified the model so that liquid-filled lung regions were those allowing reabsorbtion of tracer by the bypassing blood. In other words, we speculated that in this particular case the apneic tracer removal was fully the effects of reabsorbtion of $^{13}N_2$ by pulmonary venous blood and its lack of diffusion into liquid-filled alveoli. The data was then refitted using the dual-compartment washout equations assuming a shunt fraction of zero. The previously identified shunt fraction was set equal to the fraction of aerated (i.e., liquid-filled) blood flow to the slow-ventilated

subcompartment. The previously identified τ_S was set equal to the slow-ventilated subcompartment time constant. The model fit the washout data substantially better with an R^2 of 0.9994 (figure 6, *bottom*). From this analysis, it must be concluded that during PLV the model identifies a shunt fraction from the apneic imaging data that is the maximum possible shunt fraction. This is because during apnea the loss of tracer can be via two competing mechanisms: reabsorbtion of tracer by shunt blood flow and reabsorbtion of tracer by blood flowing from liquid-filled alveoli.

Although it is possible to introduce a third compartment, and for that matter, as many compartments as desired, the situation becomes impractical from the perspective of system identification. One might consider solving the aforementioned problem during PLV by deriving another differential equation for a liquid-filled lung compartment. This introduces one more parameter to be identified by the model, but has the shortcoming that the identified solutions lose uniqueness. Since the model fits are characterized by R^2's on the order of 0.99 or better, introducing additional parameters makes the parameter set in the model equations indeterminate. In other words, solution uniqueness is lost.

5. CONCLUSIONS

A two-compartment lumped parameter model was developed and used together with nonlinear system identification software to analyze PET imaging data collected after a single bolus injection of $^{13}N_2$-labeled saline during apnea. The model is an improvement over the analysis methods of Mijailovich et. al. [5], which primarily work for normal lungs. Thus, the model is an essential element for the single bolus injection

method. It can be used to quantify $\frac{\dot{Q}_R}{\dot{Q}_T}, \frac{\dot{Q}_S}{\dot{Q}_R}$ and $s\dot{V}_A$ directly from decay-corrected regional tracer kinetics data from masked PET images in normal *and* injured lungs. The developed model of tracer kinetics incorporates the nonlinear phenomena inherent in the PET imaging technique that include tracer transit times and PET camera signal averaging. The model's differential equations were integrated numerically using the SIMULINK package and fitted to experimental PET data to identify regional parameters from bilaterally lavaged lungs using the Nonlinear Identification Toolbox specialized software. After fitting the model to these PET functional images, we concluded from the identified parameters that PLV reduced shunt blood flow in the surfactant deficient lung.

In theory, the model should be capable of identifying the physiological parameters in a voxel-by-voxel basis. However, the signal-to-noise ratio at the voxel level is too low to provide the tracer kinetics data needed to produce accurate results with the model. Thus, we have implemented this model to study averaged ROI tracer kinetics data in numerous experimental protocols and it will continue to be used for the interpretation of our PET data. Finally, the mathematical methodology presented in this chapter can be used as a clinical diagnostic tool with human PET data to investigate and study physiologic hypotheses regarding lung disease.

Table 1. Summary (mean ± standard deviation) of parameters identified from five lavaged sheep before and after PLV.

Parameter	Bilateral Lavage			PLV		
	Nondependent	Middle	Dependent	Nondependent	Middle	Dependent
Δt_{TD} (seconds)	0.9105 ± 0.5716	1.1450 ± 0.5484	1.9420 ± 0.9342	1.0622 ± 1.2755	0.9820 ± 0.8265	1.6700 ± 0.8752
Q_R/Q_T (mL/sec)/(mL/sec)	0.0644 ± 0.0229	0.5124 ± 0.0952	0.2770 ± 0.0932	0.0616 ± 0.0233	0.4469 ± 0.1226	0.2238 ± 0.0585
Q_S/Q_R (mL/sec)/(mL/sec)	0	0.4636 ± 0.1500	0.7526 ± 0.1055	**	0.2953 ± 0.1895	0.4530 ± 0.0834
τ_s (seconds)	~	10.5018 ± 3.2749	10.5006 ± 2.6500	**	26.1445 ± 10.9119	35.9702 ± 25.9227
sV_A (sec^{-1})	0.0692 ± 0.0218	0.0983 ± 0.0282	0.0638 ± 0.0374	0.0924 ± 0.0339	0.0743 ± 0.0124	0.0153 ± 0.0041
R^2	0.9945 ± 0.0030	0.9996 ± 0.0002	0.9992 ± 0.0005	0.9966 ± 0.0014	0.9996 ± 0.0003	0.9988 ± 0.0011

** One sheep shunted activity in its nondependent ROI. $\dot{Q}_S/\dot{Q}_R$ was 14.53% and τ_S was 19.674 sec.

Table 2. Post-processed data (mean ± standard deviation) averaged for the five lavaged sheep before and after PLV.

Post-Processed Data	Bilateral Lavage			PLV		
	Nondependent	Middle	Dependent	Nondependent	Middle	Dependent
Voxels in the ROI	3879 ± 621	13092 ± 1841	6567 ± 2040	3509 ± 486	13224 ± 3130	6663 ± 2015
Shunt Fraction (Whole Lung)	0.5265 ± 0.0789			0.3252 ± 0.1392		
Relative Regional Q	0.4560 ± 0.1201	1.0779 ± 0.0545	1.1689 ± 0.1306	0.5396 ± 0.1156	1.0768 ± 0.0718	1.0882 ± 0.1493

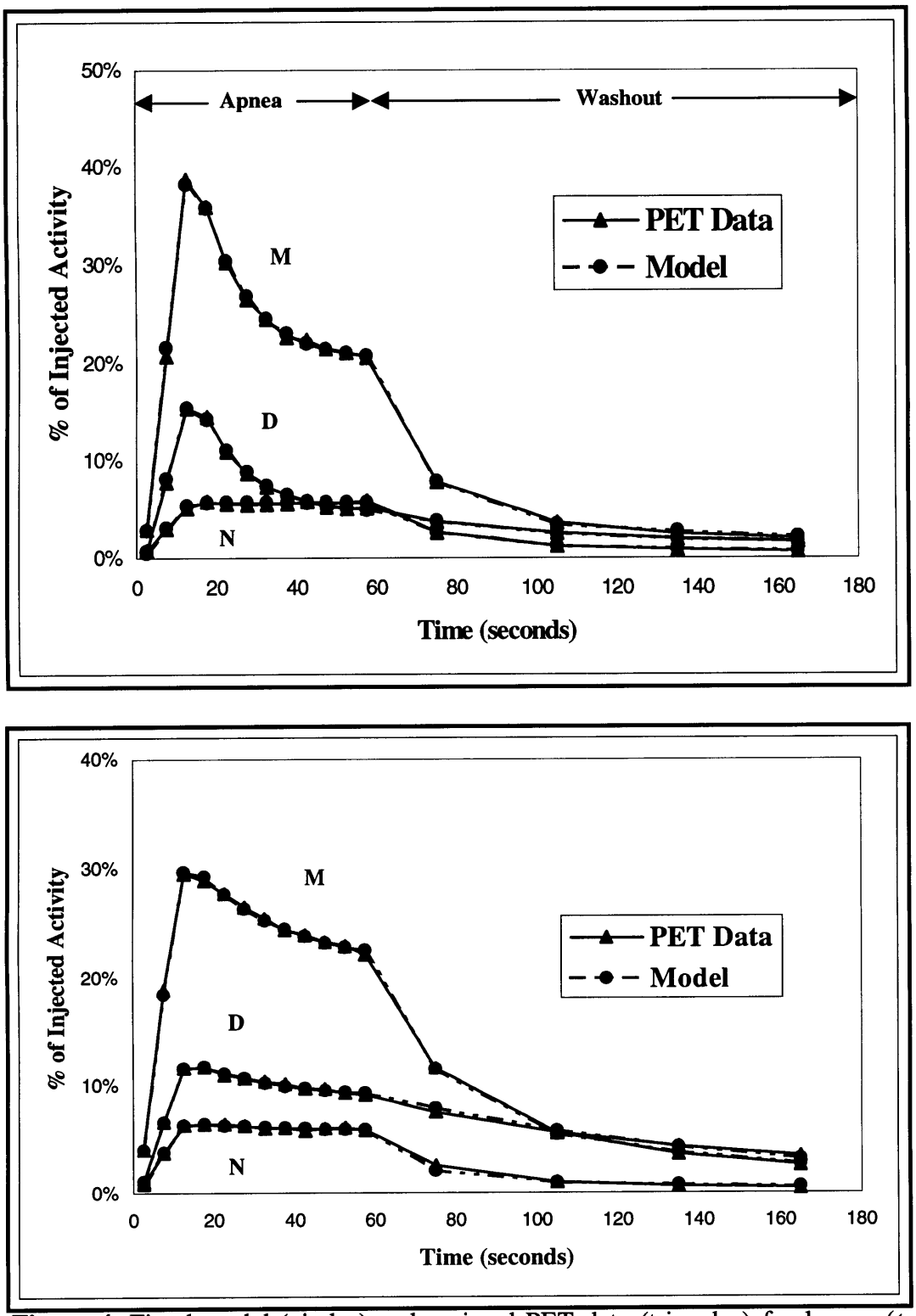

Figure 4. Fitted model (circles) and regional PET data (triangles) for lavage (*top*) and PLV (*bottom*) for the three ROI's following a $^{13}N_2$-labeled saline injection. Loss of tracer content after its peak value during apnea is lessened in the middle and dependent ROI's during PLV, consistent with the longer time constants and lower shunt fractions identified by the model (see Table 1). *D* = dependent ROI, *M* = middle ROI, N = nondependent ROI.

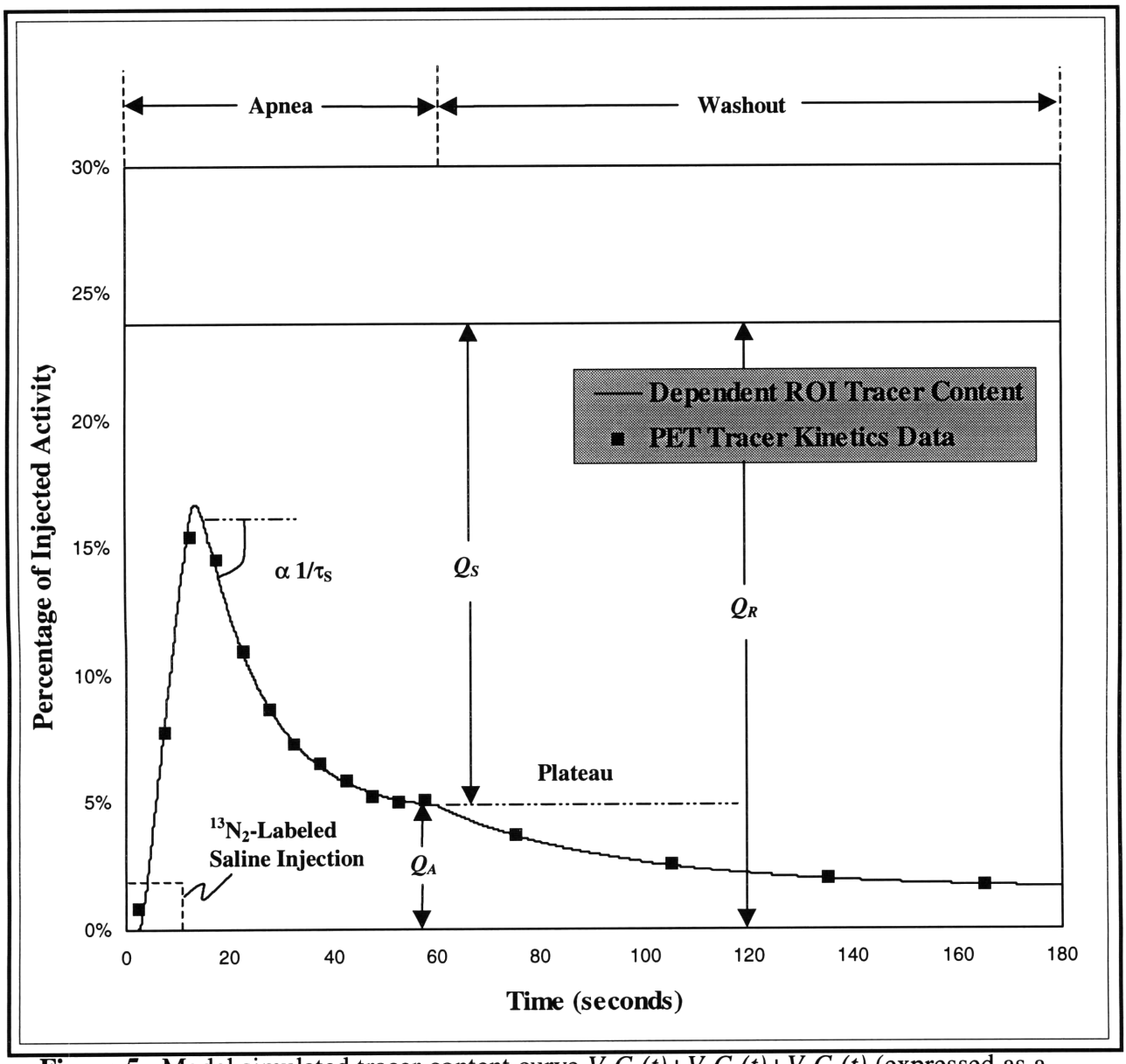

Figure 5. Model simulated tracer content curve $V_S C_S(t)+V_1 C_1(t)+V_2 C_2(t)$ (expressed as a percentage of the total injected infusate) for the dependent ROI of a bilaterally lavaged sheep lung. The tracer content appears to peak at ~16.5%, whereas the model identified regional perfusion of 23.79%. The PET tracer kinetics data is superimposed on this simulated curve, with each data point plotted at the center of its image collection time interval.

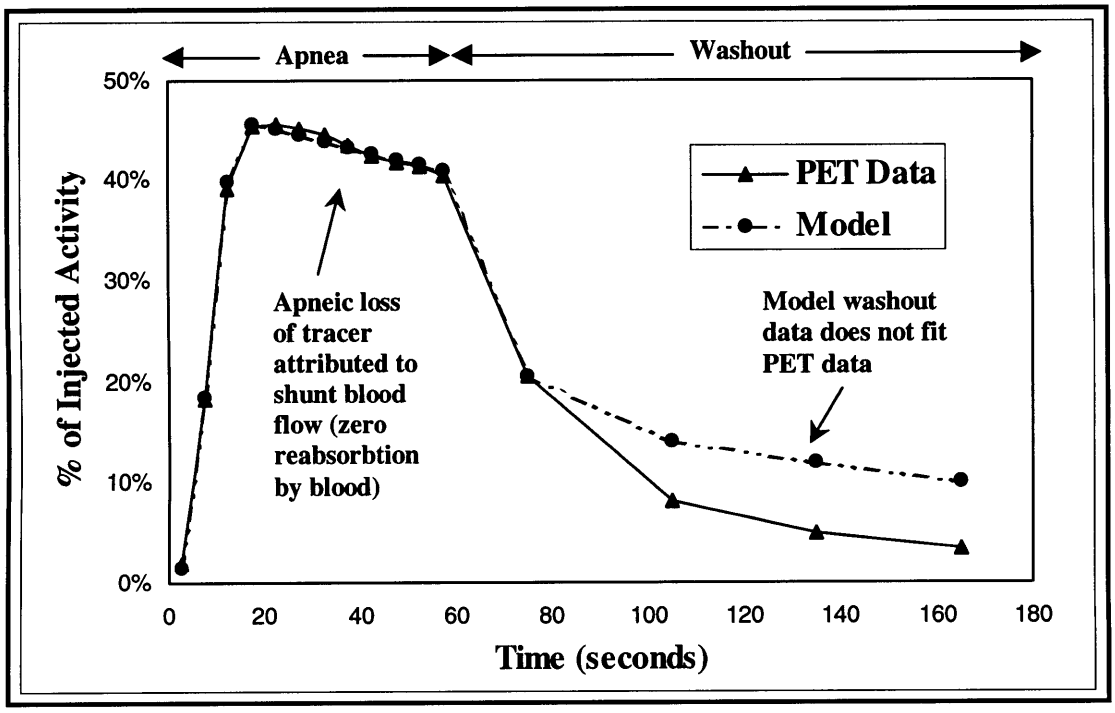

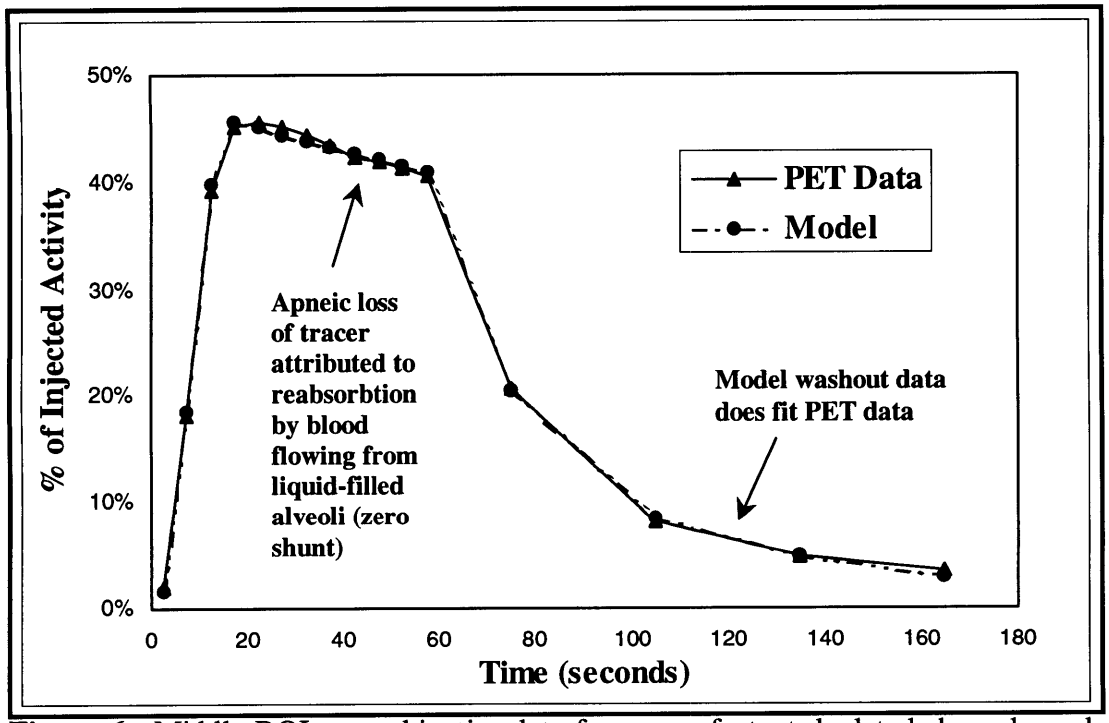

Figure 6. Middle ROI tracer kinetics data from a surfactant-depleted sheep lung during PLV with (*top*), and without (*bottom*), the assumption a zero rate constant ($1/\tau_A$) during apnea in the aerated compartment (see equation (4)). With the assumption, the fitted model data attributes loss of tracer during apnea to intrapulmonary shunt blood flow, and this activity does not ventilate during the washout ($R^2 = 0.9859$). If, instead, the loss of tracer during apnea is attributed to a nonzero $1/\tau_A$ that physically characterizes the reabsorbtion of $^{13}N_2$ gas by pulmonary venous blood flowing from liquid-filled regions, the model identifies sV_A consistent with the PET data ($R^2 = 0.9994$).

6. REFERENCES

[1] Cambridge Control Ltd. Nonlinear Identification Toolbox – User Guide. Version 1, September 1994.

[2] Cox, P.N., K.P. Morris, H. Fmdova, D. Mazer and C.McKerlie. Partial liquid ventilation (PLV) redistributes pulmonary blood flow away from dependent lung regions (Abstract). *Am. J. Respir. Crit. Care Med.* 157, *Suppl.* 3. A462, 1998.

[3] Harris, R.S., D.B. Willey-Courand, C.A. Head, G.G. Galletti and J.G. Venegas. Effects of pulmonary vasodilation on regional perfusion (Q_r) and ventilation (V_{Ar}) during partial liquid ventilation (PLV) (Abstract). *Am. J. Respir. Crit. Care Med.* 157, *Suppl.* 3. A462, 1998.

[4] Klocke, R.A. Ventilation, Pulmonary Blood Flow and Gas Exchange. *Pulmonary Diseases and Disorders*, 2nd Edition. McGraw-Hill Book Company, New York, 185-198, 1988.

[5] Mijailovich, S.M., Steven Treppo and Jose G. Venegas. Effects of lung motion and tracer kinetics corrections on PET imaging of pulmonary function. *J. Appl. Phsyiol.* 82: 1154-1162, 1997.

[6] Rhodes, C.G., Valind, S.O., Brudin, L.H., Wollmer, P.E., Jones, T. and Hughes, J.M.B. Quantification of regional $\dot{V}_A/Q$ ratios in humans by use of PET. I. Theory. *J. Appl. Physiol.* 66:1896-1904, 1989.

[7] Rhodes, C.G., Valind, S.O., Brudin, L.H., Wollmer, P.E., Jones, T. and Hughes, J.M.B. Quantification of regional $\dot{V}_A/Q$ ratios in humans by use of PET. II. Procedure and normal values. *J. Appl. Physiol.* 66:1905-1913, 1989.

[8] Schuster, D.P. Positron emission tomography: theory and its application to the study of lung disease. *Am. Rev. Respir. Dis.* 139: 818-840, 1989.

[9] Seow, D. Quantification of intrapulmonary blood shunt and ventilation/perfusion distributions in injured lungs by Positron Emission Tomography. Mechanical Engineering Master Thesis, Department of Mechanical Engineering, MIT. 1995.

[10] Shaffer, T.H. A brief review: liquid ventilation. *Undersea Biomedical Research.* Vol. 14, No. 2, March 1987.

[11] Simon, B.A. and Venegas, J.G. Analyzing ^{13}NN washout curves in the presence of intraregional nonuniformities. *J. Appl. Physiol.* 76(2): 956-964, 1994.

[12] Treppo, S., S.M. Mijailovich and J.G. Venegas. Contributions of pulmonary perfusion and ventilation to heterogeneity in $\dot{V}_A/Q$ measured by PET. *J. Appl. Physiol.* 82: 1163-1176, 1997.

[13] Treppo, S. Quantification of pulmonary perfusion, ventilation and the ventilation/perfusion ratio by Positron Emission Tomography. Mechanical Engineering Master Thesis, Department of Mechanical Engineering, MIT. 1994.

[14] Venegas, J.G. , R.S. Harris, G.G. Galletti, D.B. Willey and C.A. Head. Partial liquid ventilation (PLV) decreases shunt and not perfusion to dependent lung regions in oleic acid induced ARDS (Abstract). *Am. J. Respir. Crit. Care Med.* 155, *Suppl.* 4, pt. 2: A745, 1997.

[15] West, J.B. *Respiratory Physiology – the essentials*, 5th Edition, Williams and Wilkins, New York, 1995.

[16] Willey, D.B., R.S. Harris, C.A. Head, G.G. Galletti and J.G. Venegas. Relative perfusion (Q_r), shunt fraction (Q_s/Q_r) and ventilation ($\dot{V}_A$) inequalities during oleic acid induced ARDS as measured with PET (Abstract). *Am. J. Respir. Crit. Care Med.* 155, *Suppl.* 4, pt. 2: A745, 1997.

[17] Willey-Courand, D.B., R.S. Harris, G.G. Galletti, C. Hales and J.G. Venegas. Alterations of regional ventilation and perfusion after smoke inhalation (Abstract). *Am. J. Respir. Crit. Care Med.*157, *Suppl.* 3. A367, 1998.

[18] Willey-Courand, D.B. R.S. Harris, G.G. Galletti, C.A. Head and J.G. Venegas. Partial liquid ventilation (PLV) reduces shunt (Q_s/Q_T) in the surfactant deficient Lung (Abstract). *Am. J. Respir. Crit. Care Med.*157, *Suppl.* 3. A464, 1998.

CHAPTER 2

FRACTAL ANALYSIS OF POSITRON EMISSION TOMOGRAPHY IMAGES OF PULMONARY BLOOD FLOW

ABSTRACT

Fractal systems exhibit characteristic patterns that are independent of magnification or scale. The pulmonary vasculature is fractal in nature, and the spatial distribution of pulmonary perfusion has been characterized using fractal models. One method to estimate fractal dimension involves the calculation of spatial heterogeneity as a function of measuring resolution scale. An implementation of this method involves slicing the excised lung into cubic pieces after it has been perfused with labeled microspheres [3][5]. This approach has inherent limitations. Increasing measuring resolution scale causes peripheral perfusion data to be excluded from the analysis because it contains extrapulmonary regions. Furthermore, misregistration artifacts may theoretically affect the recovered fractal dimension when the sampling grid is offset relative to the self-similar fractal pattern or is not an exact integer scale of that pattern. We hypothesize that two-dimensional low-pass filtering could be used as a method to assess the fractal dimension of pulmonary perfusion measured by Positron Emission Tomography (PET). In this method, the resolution scale would be inversely proportional to the corner frequency of the low-pass filter used. The method was tested against three types of images: random noise images, synthetic fractal images, and PET images of pulmonary perfusion. Images were processed with two-dimensional low-pass filters of decreasing corner frequencies, and a spatial heterogeneity index ($\mathrm{cov} = \frac{\sigma}{\bar{x}}$) was

calculated for each low-pass filtered image. The natural logarithm of the coefficient of variation scaled linearly with the natural logarithm of resolution scale for the PET images studied, with an average linear regression coefficient (R^2) of 0.99. Fractal dimensions ranged from 1.25 to 1.36 for the distribution of pulmonary perfusion adjusted by removing vertical gradients. For the same data before removing the effect of vertical gradients, *D* ranged from 1.11 to 1.14 with an average R^2 of 0.96. We conclude that the proposed methodology may be used to estimate the fractal dimension from PET functional images of perfusion. The method includes all data in the lung field, and is insensitive to the effects of misregistration. A relationship between the fractal dimension of two-dimensional functional images and their power spectral density offers new insights into the interpretation of the fractal dimension as a measure of the frequency content of spatial heterogeneity.

1. INTRODUCTION

The distribution of pulmonary blood flow has been characterized in several species using fractal models [1][2][3][4][5]. The method used to characterize the fractal dimension involves plotting spatial heterogeneity of blood flow as a function of the spatial resolution scale used to make the measurement [1]. Mathematically, if the distribution of a functional variable is fractal, then a constant relationship must exist between the heterogeneity of that variable (*X(R)*) and a power of the resolution scale (*R*) used to measure that variable:

$$\frac{X(R)}{X(R_o)} = \left(\frac{R}{R_o}\right)^{1-D} \qquad (1)$$

where R_o is an arbitrary resolution scale used as a reference point and D is the spatial fractal dimension. A parameter used commonly to quantify spatial heterogeneity is the coefficient of variation (*cov*), defined as the standard deviation of the data (σ) normalized by its mean ($\bar{x}$).

$$\text{cov} = \frac{\sigma}{\bar{x}}$$

Pulmonary perfusion heterogeneity in the lungs has been measured from the distribution of intravenously injected radiolabeled or fluorescent microspheres into the pulmonary circulation [3][5]. Microspheres, with diameter (10μm) larger than the pulmonary capillary, are thought to deposit in small arterioles of the lung in direct proportion to local blood flow. The animal subject is then sacrificed, and the lungs are excised, dried, and sliced into uniformly sized cubic pieces. *cov* is calculated for increasingly larger resolution scales by grouping adjacent pieces into progressively larger cubes. A limitation of this method is that increasing cube size causes the exclusion of peripheral data that would incorporate pieces outside the lung. Furthermore, the evaluation of the fractal dimension via this method may be theoretically subject to artifacts such as misregistration between the measuring grid and the physiologic structure: the grid and the organ do not have the same geometric shape, may not be an integer multiple size of the fractal pattern, or may have an offset relative to the fractal pattern.

We investigated an alternative method to assess the fractal dimension of functional heterogeneity measured with tomographic imaging. We theorized that two-dimensional low-pass filtering a functional image could be used to assess its fractal dimension, given that the corner frequency of the low-pass filter should be inversely related to the resolution scale. An advantage of this method is that no data needs to be

excluded from the analysis. In this study, the low-pass filtering method was evaluated in three types of images: random noise images in the shape of the lungs, synthetically generated fractal images, and PET images of pulmonary blood flow.

2. METHODS

2.1. Measuring the Fractal Dimension

The spatial heterogeneity of a three-dimensional or two-dimensional data set can be characterized as a function of the measuring scale size. In equation (1), we replace the measuring scale size (R) by $\left(\frac{1}{f_c}\right)^2$ and the property X by the coefficient of variation (cov) of the data set after filtering it with a corner frequency f_c ($\mathrm{cov}(f_c)$).

$$\frac{\mathrm{cov}(f_c)}{\mathrm{cov}(f_{c,o})} = \left[\frac{\left(\frac{1}{f_c}\right)^2}{\left(\frac{1}{f_{c,o}}\right)^2}\right]^{(1-D)} \tag{2}$$

In the conventional method, a characteristic volume defines the measuring scale size used for analyzing a three-dimensional data set. By analogy, in a two-dimensional data set, the measuring scale size can be defined by a characteristic area which, in the case of the low-pass filtering method, corresponds to the square power of the inverse of the filter's corner frequency $\left(\frac{1}{f_c}\right)^2$.

Taking the natural logarithm of both sides of equation (2) and rearranging gives a linear relationship between $\ln(\mathrm{cov}(f_c))$ and $\left(\frac{1}{f_c}\right)$.

$$\ln\left(\mathrm{cov}\left(f_c\right)\right) = 2(1-D)\times \ln\left(\frac{f_{c,o}}{f_c}\right) + \ln\left(\mathrm{cov}\left(f_{c,o}\right)\right) \quad (3)$$

The fractal dimension of a two-dimensional functional image can thus be estimated from the slope (m) of a log-log plot between *cov* and $\frac{1}{f_c}$.

$$D = 1 - \frac{m}{2} \quad (4)$$

To test the hypothesis, the two-dimensional low-pass filtering method was applied to three types of images: random noise images, synthetic fractal images, and PET images of pulmonary perfusion, described below.

2.1.1. Random Noise Images

Random noise images were created in the shape and size of a typical dog lung cross-section using a random number generator that produced random voxel elements chosen from a normal distribution with a mean of zero and variance of 1.0. One hundred different noise images were analyzed. For each noise image, a log-log plot of *cov* versus $\frac{1}{f_c}$ was generated, and the fractal dimension and R^2 of the least-squares fit regression line were calculated.

2.1.2. Synthetic Two-Dimensional Fractal Images

Synthetic fractal images were created by dividing a square-shaped unity matrix (size: 128×128 voxels) into four identical squares and multiplying these by the corresponding element of a 2×2-similarity matrix, in which the sum of its four elements was unity. Each of the four squares was further subdivided into four, and each multiplied

by the corresponding elements in the 2×2 matrix. The process was repeated until the smallest subdivision was of size 2×2: the size of the similarity matrix (figure 1).

These synthetic fractal images were used to compare the results obtained using the conventional method of estimating the fractal dimension D to those obtained using the two-dimensional low-pass filtering method. The conventional method was simulated by successively grouping data into adjacent squares of equal size, and calculating the *cov* of the corresponding averages. The process was repeated for larger and larger grouping squares until the fractal image consisted of four squares. Resolution scale size was taken as the area of the grouping squares in number of voxels. Fractal dimensions were obtained from the equation: $\ln \mathrm{cov}(n_v) = 2(1-D)\ln\left(\frac{n_v}{n_{v,o}}\right) + \ln \mathrm{cov}(n_{v,o})$, where n_v is the number of voxels making the side of the square piece and $n_{v,o}$ is the side length in voxels of the smallest square used.

To simulate the artifacts created by misregistration between the fractal pattern and measuring grid in the conventional method, an initial measuring scale of 3×3 voxels was used in the fractal image. The size of the measuring scale was then progressively increased by factors of 2 (6×6, 12×12, etc.) relative to the size 2×2 fractal pattern. Squares including voxels outside the square fractal image were not included in the calculation. Each synthetic fractal image was also analyzed with the low-pass filtering method described above.

To estimate the extent of the artifact created by misalignment between the fractal pattern and the measuring grid, the fractal images were padded with one row of zeros on all four sides. An initial misalignment of one voxel was allowed between the fractal

pattern and the measuring grid of 2×2 squares. Keeping the same misalignment, the size of the measuring grid was progressively increased by factors of two. Grouping squares including voxels outside of the fractal image were not included in the analysis. The padded fractal image was also analyzed with the low-pass filtering method, and fractal dimensions obtained with each method were recorded.

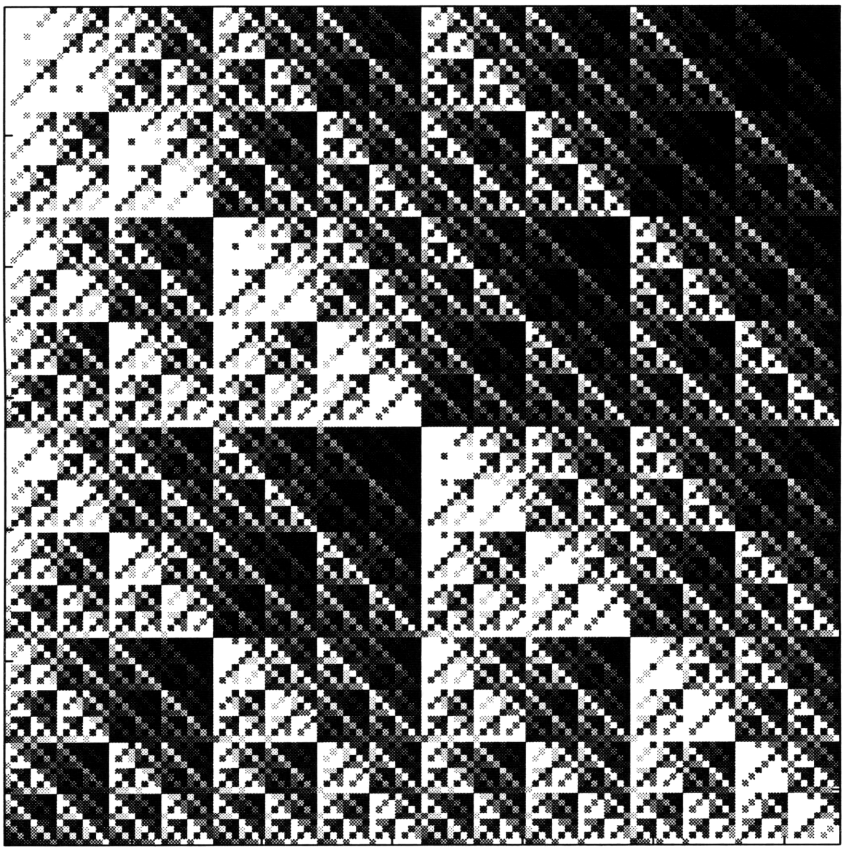

Figure 1. Square-shaped synthetic fractal image (size: 128×128 voxels) used to compare fractal dimensions, *D*, using the conventional method and the low-pass filtering method.

2.1.3. PET Images of Pulmonary Perfusion

2.1.3.1. Methodology

A PET camera was used to image pulmonary perfusion ($\dot{Q}$) in 6 anesthetized and mechanically ventilated supine dogs with normal lungs. The method to assess local $\dot{Q}$ consisted of stopping ventilation at end exhalation and injecting a bolus of $^{13}N_2$-labeled saline into a jugular vein catheter. Infusion time ranged between 10 to 15 seconds, depending on the specific activity of the infusate (100 to 400 μCi/mL) to produce images with consistent levels of radioactivity per voxel. The collection of a series of 6 sequential PET images (each of 10 seconds in duration) was initiated simultaneously with the beginning of infusion and the interruption of mechanical ventilation. Given the low solubility of $^{13}N_2$ gas in blood and tissues (partition coefficient λ equal to 0.018), in these normal lungs virtually all radioactivity was transferred to aerated alveoli at first pass, and regional tracer content was proportional to local perfusion [6]. At the end of the 60 seconds of apnea, mechanical ventilation was restarted and the tracer washed out.

2.1.3.2. Image Processing and Analysis

Original sinograms were reconstructed with the convolution-back projection algorithm giving images with the highest spatial resolution of the PET camera (7 mm). Image reconstruction included corrections for nonuniform crystal sensitivity and gamma-ray energy attenuation caused by animal tissue and camera supporting structures. Since, in these normal lungs, minimal changes in alveolar airspace concentration occurs after the arrival of the tracer, the last four reconstructed images in the protocol were added together to create an image of pulmonary perfusion.

A significant portion of the image heterogeneity is caused by a gradient in the vertical direction, which is superimposed to the expected fractal pattern. To remove this gradient from the images, the best-fit vertical gradient plane was obtained by linear regression and subtracted from the original image. The resulting image represented non-vertical residual spatial heterogeneity and was submitted to the fractal analysis. Surface plots of a representative perfusion image, its vertical gradient plane, and the residual image are shown in figure (2).

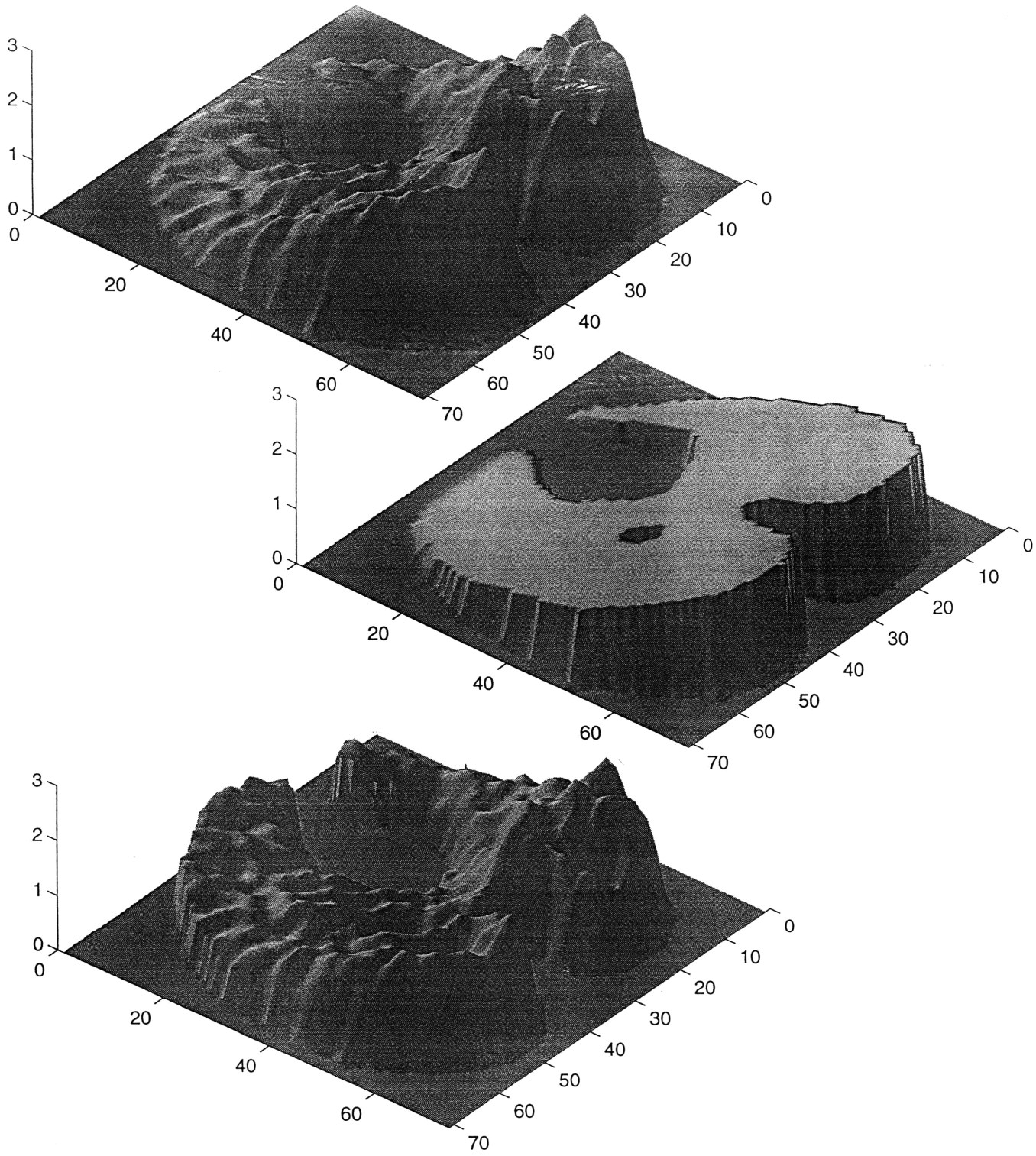

Figure 2. Perfusion cross-sectional image presented as an illuminated surface plot where the height above the *x-y* plane represents the relative magnitude of regional perfusion (*top*). The gradient plane (*middle*) was subtracted from the original image, resulting in the residual image (*bottom*) used in the fractal analysis.

2.2. Filter Design Methodology and Edge Effects

Application of a two-dimensional low-pass filter to an image ideally produces an image where all frequencies higher than the cutoff frequency are removed from it. The cutoff frequency of a filter is generally expressed as a proportion of the Nyquist frequency (f_N), which corresponds to ½ of the number of voxels per unit length. The perfusion images analyzed in this study were collected with a multiple slice PET camera with an intrinsic resolution length of 7 mm and a voxel size of 2×2 mm with slice thickness of 6 mm (Nyquist frequency is equal to $\frac{1}{2}\times\left(\frac{1}{2}mm^{-1}\right)=\frac{1}{4}mm^{-1}$). Low-pass filters with corner frequencies ranging from $0.02f_N$ to $0.55f_N$ were used. The lowest frequency, $0.02f_N$, corresponds to a wavelength roughly equal to twice the maximum diameter of the thorax of our animals. The highest frequency, $0.55f_N$, is higher than $0.28f_N$, the wavelength corresponding to the spatial resolution of the PET camera (3.5 voxels = 7 mm). Residual perfusion images were analyzed for nineteen corner frequencies in the range of $0.02f_N$ to $0.55f_N$.

A problem inherent with low-pass filtering an image is an artifactual smearing of the sharp edges. Measured spatial heterogeneity is artifactually overestimated as corner frequency is decreased because smeared edges are included in the region of interest. Thus, using the low-pass filtering method without correction should result in erroneous measures of the fractal dimension. Edge effects were minimized using the following technique. First, a lung mask was created containing ones in all voxels inside the lung field and 0's outside. This unity mask was multiplied to the low-pass filtered functional image to set voxels outside of the lung to zero. The unity mask was then filtered with the

same low-pass filter applied to the functional image and the resulting filtered mask was used to normalize the filtered functional image. *cov* was then calculated from these processed images. Because the edge effects of filtering were proportionally equivalent on the functional image and the unity mask, normalization of the former virtually eliminated these edge effects (figure 3).

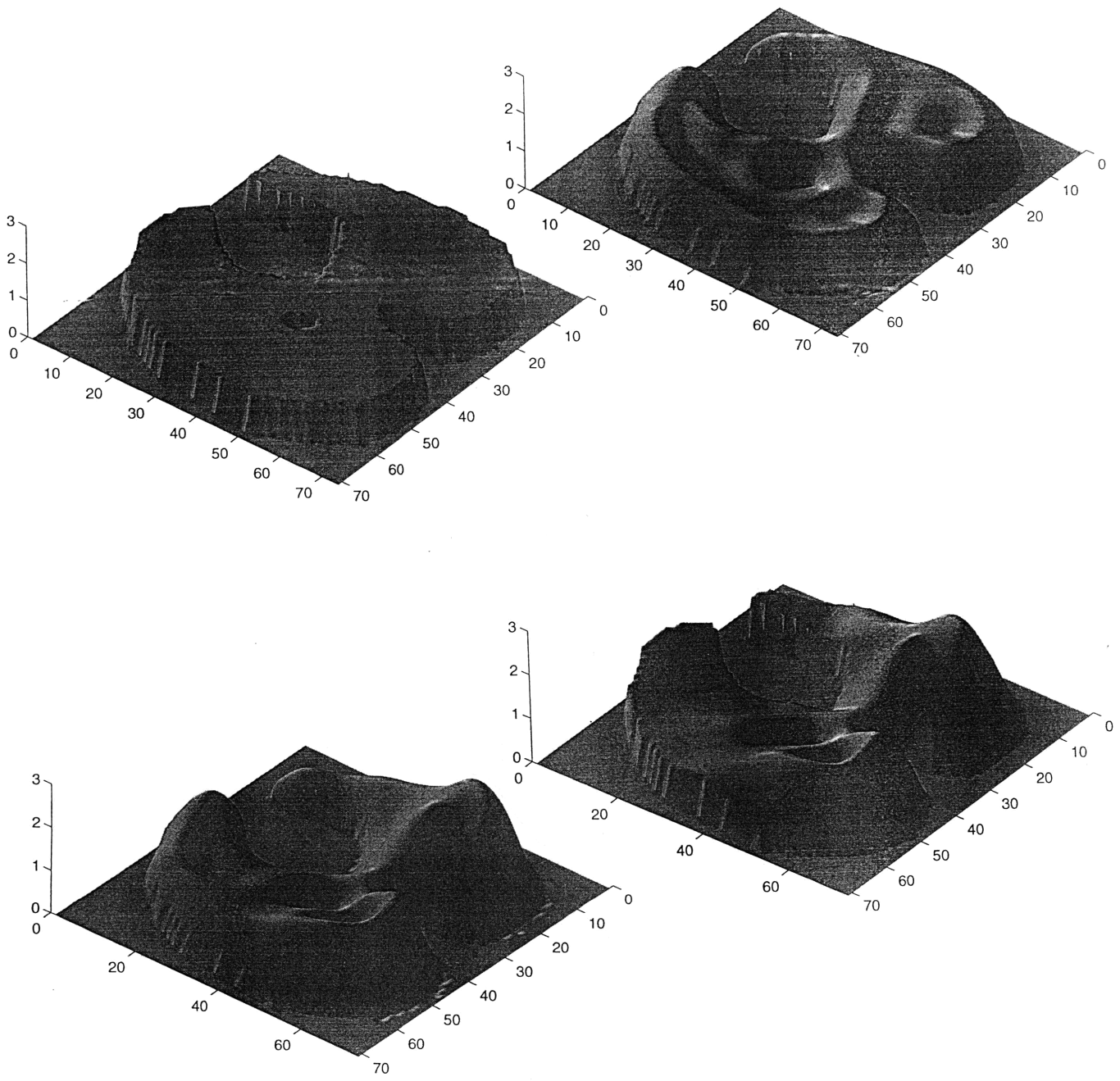

Figure 3. Unity mask corresponding to the images in figure (2) presented as an illuminated surface plot (*top left*). Low-pass filtered unity mask with $f_c = 0.1675 f_N$ multiplied to the unity mask (*top right*). Residual image of figure (2) low-pass filtered with $f_c = 0.1675 f_N$ before correction (*bottom left*), showing smeared edges. After correction by normalization with the filtered unity mask multiplied to the unity mask, image edges are restored (*bottom right*).

3. RESULTS

(a) Random noise images

One hundred random noise images cast in the shape and size of a typical dog lung cross-section and analyzed with the low-pass filtering method yielded linear relations between $\ln(\mathrm{cov}(f_c))$ and $\ln\left(\frac{1}{f_c}\right)$ with an average R^2 of 0.9986 and D of 1.5045 ± 0.0257, not statistically different from 1.5 (figure 4).

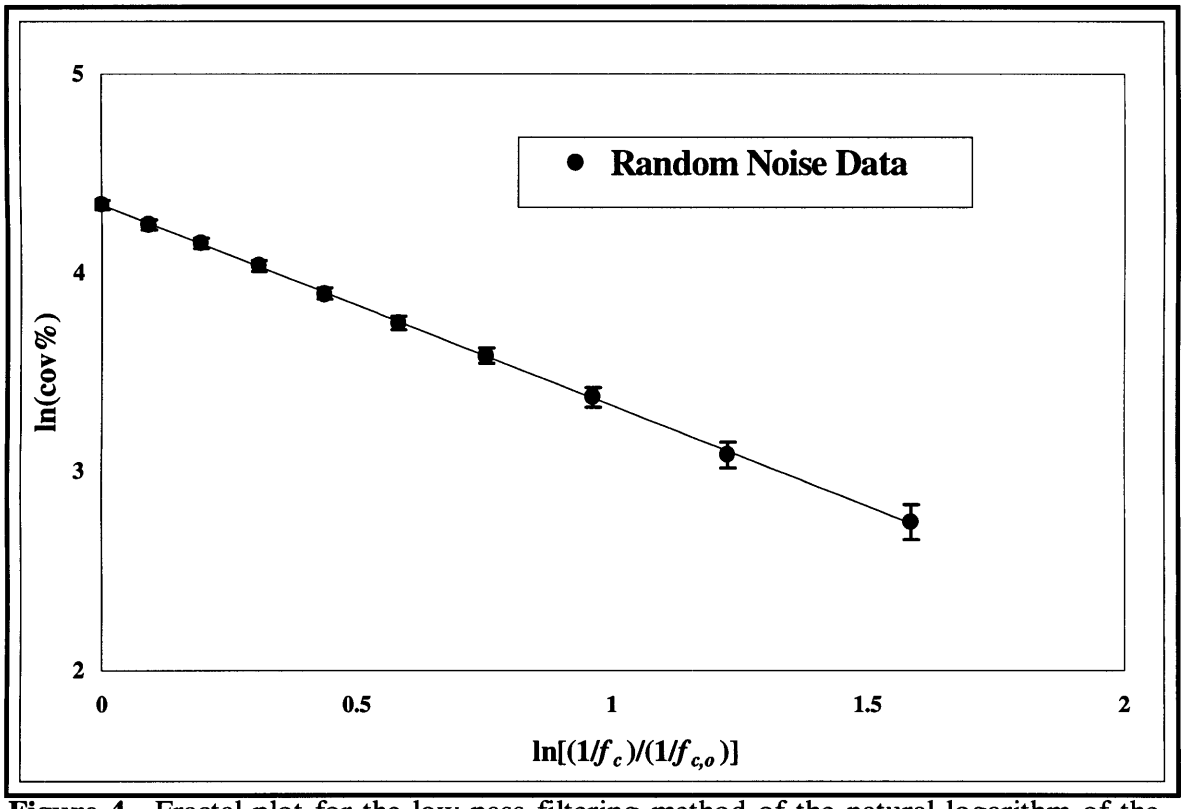

Figure 4. Fractal plot for the low-pass filtering method of the natural logarithm of the *cov* vs. the natural logarithm of the normalized inverse corner frequency of the filter. Method was applied to one hundred random noise images cast in the shape and size of a typical dog lung cross section. The average ln(*cov*%) for the one hundred images was calculated per low-pass filter corner frequency (f_c). Error bars indicate ± standard deviation for each data point. A linear regression fit through the data in this figure yielded D of 1.5045 with an R^2 of 0.9998.

(b) Synthetic fractal images

As expected, application of the conventional method and the low-pass filtering method to the synthetically generated fractal images blurred them with increasing resolution scale (figure 5). The conventional method yielded three different fractal dimensions for the same fractal image as a result of misregistration (figure 6). The perfectly registered 2×2 starting grid yielded D of 1.16 with R^2 of 0.9625. The misregistered starting grid, size 3×3, yielded a D of 1.17 with an R^2 of 0.9531. The misaligned 2×2 grid offset by 1 voxel yielded a D of 1.10 with an R^2 of 0.9491. The same synthetic fractal image was processed with the filtering method. Both the original image and that shifted by zero padding yielded an identical D of 1.13 both with R^2 of 0.9921, demonstrating the insensitivity of the method to misregistration (figure 7).

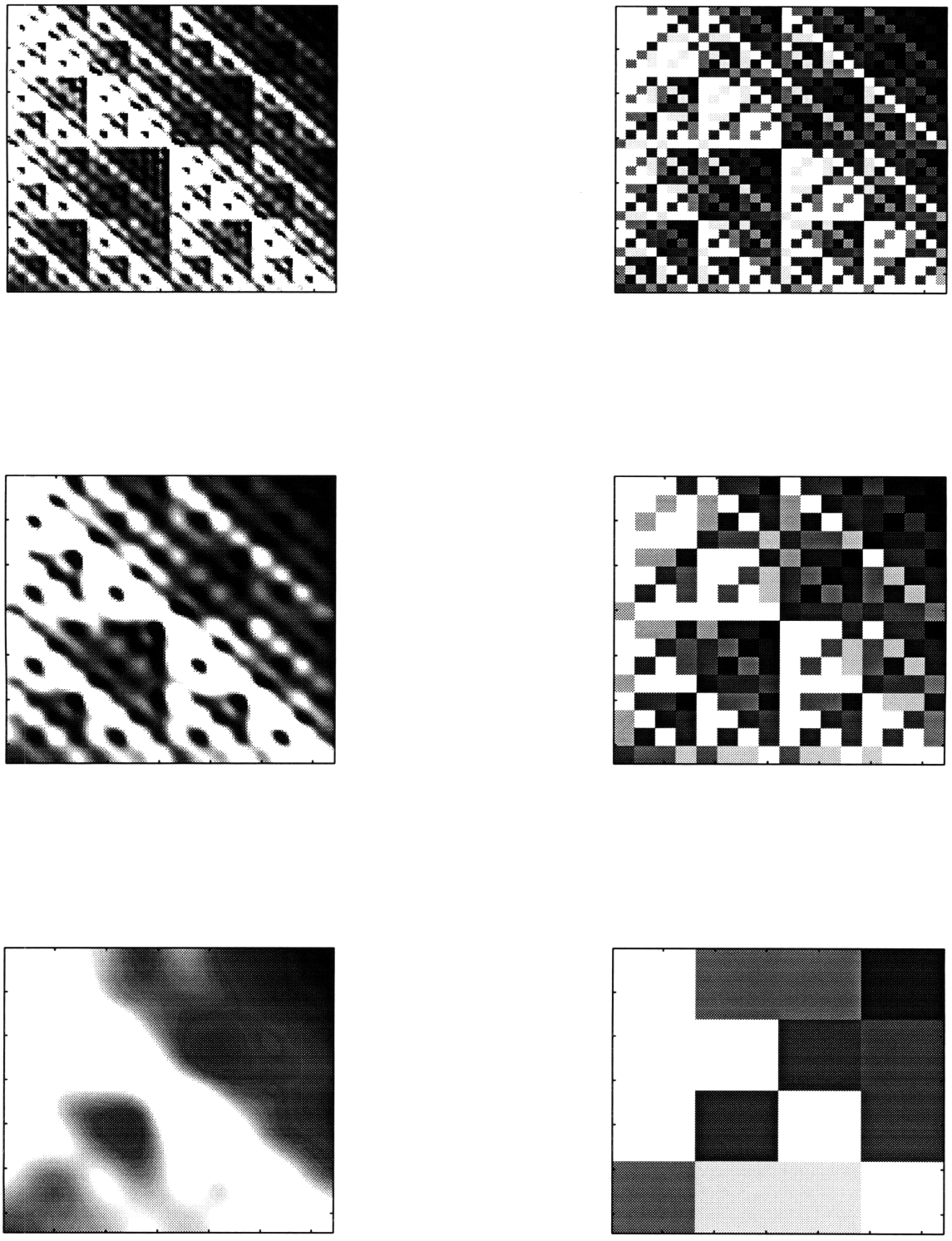

Figure 5. Synthetic fractal image of figure (1) processed with the low-pass filtering method (*left column*) and conventional method (*right column*) with increasing resolution scale (top to bottom). For the low-pass filtering method, the image was filtered with f_c of $0.492f_N$, $0.2265f_N$ and $0.0498f_N$, respectively. For the conventional method, side lengths of the grouping squares in number of voxels were 4, 8 and 32 voxels, respectively.

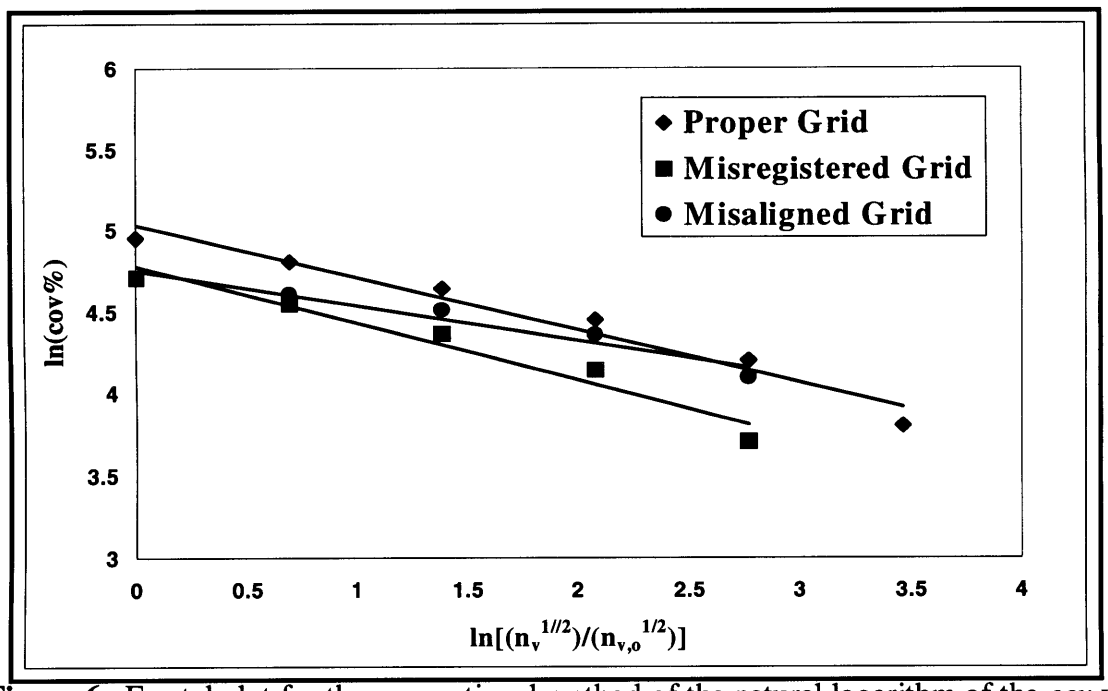

Figure 6. Fractal plot for the conventional method of the natural logarithm of the *cov* vs. the natural logarithm of the square root of the number of voxels in a square piece applied to the synthetic fractal image of figure (1). Three different grids were used: proper grid (◆), misregistered grid (■), and a misaligned grid (●).

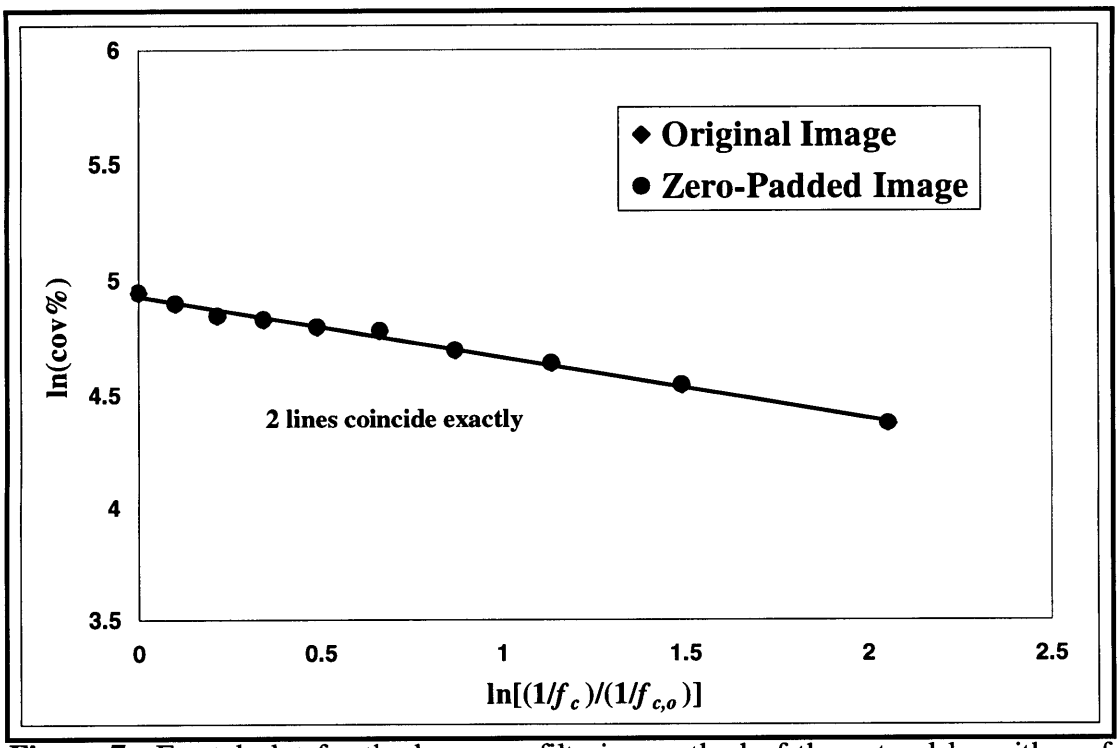

Figure 7. Fractal plot for the low-pass filtering method of the natural logarithm of the *cov* vs. the natural logarithm of the normalized inverse corner frequency of the filter. Method was applied to the synthetic fractal image of figure (1) for an original image (◆) and one displaced by one voxel by padding with zeros (●). The two best-fit lines coincide exactly, irrespective of zero padding.

(c) PET images of pulmonary perfusion

A plateau was reached in the plot of spatial heterogeneity ($\ln(cov\%)$) versus normalized resolution scale ($\ln[(1/f_c)/(1/f_{c,o})]$) for $\left(\frac{1}{f_c}\right) < \left(\frac{1}{0.28 f_N}\right)$. This corresponds to the theoretical spatial resolution of the PET camera. For $\left(\frac{1}{f_c}\right) > \left(\frac{1}{0.28 f_N}\right)$, the data followed a linear relationship with an average R^2 of 0.99 (figure 8). Fractal dimensions for pulmonary perfusion ranged from 1.25 to 1.36, with an average of 1.31 (table 1).

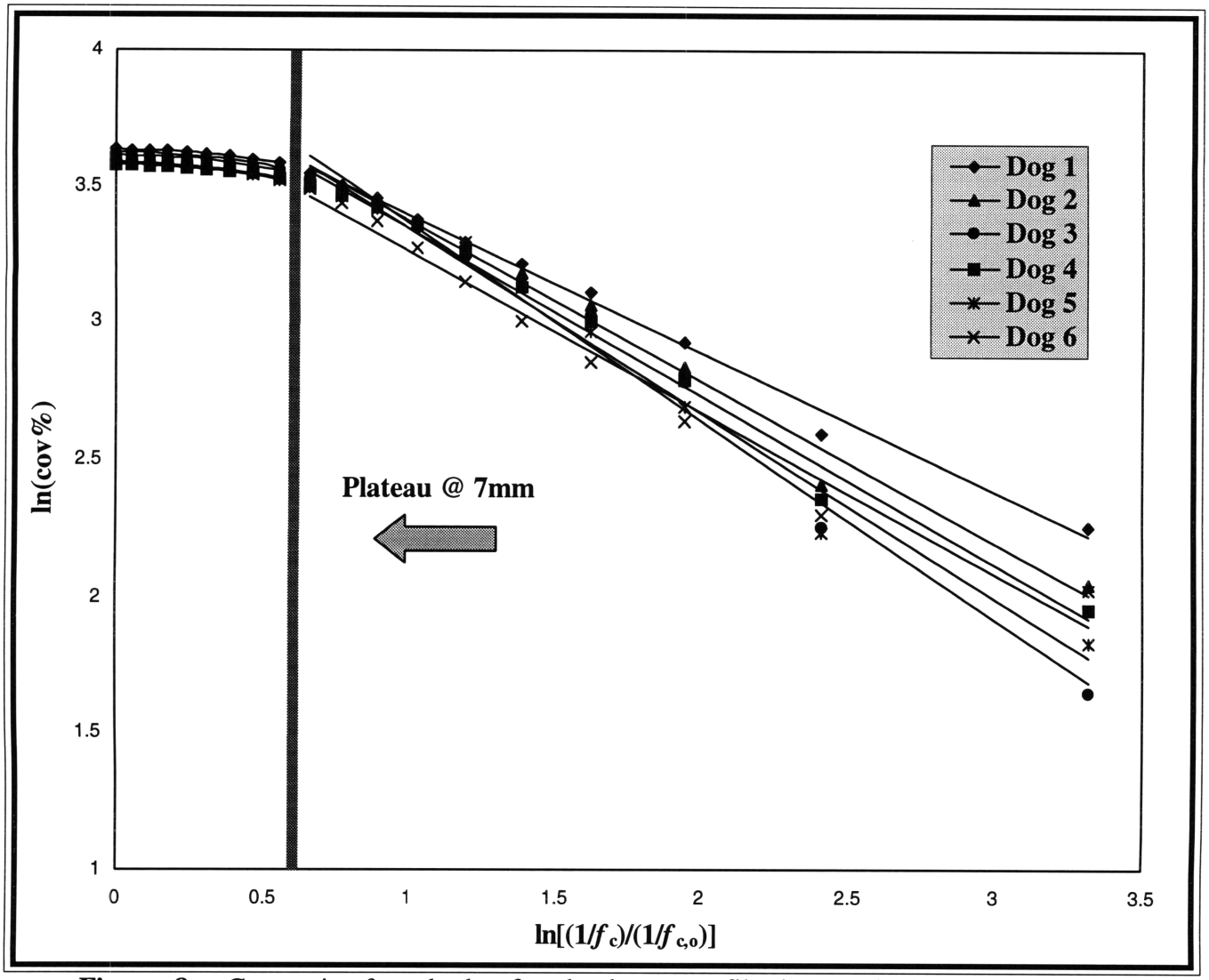

Figure 8. Composite fractal plot for the low-pass filtering method of the natural logarithm of the *cov* vs. the natural logarithm of the normalized inverse corner frequency of the filter for six normal dogs lying supine. Note that inflection towards a plateau occurs at the same spatial frequency for all dogs, which corresponds to the intrinsic spatial resolution of the PET camera.

Table 1. Fractal dimensions (D) and R^2's for the 6 dogs.

Dog	Fractal Dimension (D)	R^2 for $\ln(f_{c,o}/f_c) > 0.68$
Dog 1	1.25	0.99
Dog 2	1.30	0.99
Dog 3	1.36	0.99
Dog 4	1.31	0.99
Dog 5	1.34	0.98
Dog 6	1.29	0.98
Average	1.31	0.99

4. DISCUSSION

The most important findings of this study are:

1. Low-pass filtering of PET functional images can be used to change the resolution scale at which their spatial heterogeneity is calculated, and thus the low-pass filtering method can be used to calculate their fractal dimension. The need to exclude any data with this method is eliminated.
2. Normalization of low-pass filtered images by equivalently filtered unity masks minimizes edge-smearing effects inherently created by filtering.
3. For all PET perfusion images studied, spatial heterogeneity ceased to increase when resolution scale was reduced to below the intrinsic spatial resolution of the PET camera.
4. Our average fractal dimension D for PET perfusion images in dogs after removing vertical gradients was 1.31 with a good linear correlation ($R^2 = 0.99$).
5. Vertical gradients in perfusion seem to have a substantial effect on the estimate of D and offset the linearity between spatial heterogeneity and resolution scale.

PET Imaging Methodology for the in vivo Measurement of Pulmonary Perfusion. The underlying assumption for the fractal analysis of blood flow heterogeneity can be generalized: systemic and pulmonary vascular trees are fractal in nature and thus the spatial distribution of intraorgan blood flow should also be fractal. Application of equation (1) to calculate the fractal dimension thus requires that experimental measurements of blood flow accurately represent its spatial distribution. Pulmonary blood flow has been measured from the spatial distribution of $^{13}N_2$ measured by PET following an intravenous injection of $^{13}N_2$-labeled saline. Given the high insolubility of the $^{13}N_2$ gas, migration of the tracer labeled blood in the pulmonary capillary vessels to alveolar airspace is virtually completed. With the assumption that the $^{13}N_2$ gas remains approximately stationary in the airspace during apneic imaging, thoracic tracer content at the voxel level is proportional to local blood flow [6].

Physical Interpretation of the Synthetic Fractal Images. The synthetically generated fractal images can be considered as an idealization of a two-dimensional perfusion image from a lung where each parent blood vessel distributes flow to four daughter branches in constant proportions. These images are in effect equivalent to the fractal dichotomous model proposed by Glenny and Robertson [4] to explain the fractal properties of the blood flow distribution. We used four instead of two subdivisions at each parent-to-daughter generation to simplify the computation in generating the two-dimensional image.

Low-Pass Filtering Methodology and Minimization of Edge Effects. The application of the low-pass filtering method for the fractal analysis of images was possible because of the inverse proportionality between resolution scale and corner frequency. Changing the

resolution at which spatial heterogeneity is measured is equivalent to changing low-pass filter corner frequency. A low-pass filter removes high spatial frequency components from images resulting in a blurring effect. This blurring is magnified as the filter's corner frequency is decreased, an effect analogous to that of increasing the size of volumetric tissue pieces in the conventional method.

Two major advantages of the low-pass filtering method over the conventional method ensure a more robust calculation of the fractal dimension. Firstly, the low-pass filtering method is insensitive to misregistration, artifacts associated with the conventional method. The low-pass filtering method does not require alignment between a measuring scale grid with the governing fractal pattern of an image. Secondly, the low-pass filtering method does not exclude any data from the analysis. Artifactual smearing of image edges created by low-pass filtering might lead one to believe that the low-pass filtering method and the conventional method share a common problem: the need to exclude peripheral data with large resolution scales. However, by using our normalization technique the smearing of image edges is minimized and all data in the lung field can be used in the calculation of the spatial heterogeneity at every level of resolution.

Without a correction method for smeared edges, an artifact that is inherently created when images are filtered, the low-pass filtering method cannot be applied. The degree of distortion of the image edges is exaggerated as corner frequency is decreased. This induces increased artifactual heterogeneity. The effectiveness of the correction method that we applied to minimize edge smearing is best exemplified in a random noise image. With correction for edge smearing, the expected linearity ($R^2 = 0.9997$) and approximate fractal dimension ($D = 1.53$) are obtained from the fractal plot of ln(*cov*%) versus

$\ln[(1/f_c)/(1/f_{c,o})]$ (figure 9). Without correction, artifactual heterogeneity increases with increasing $(1/f_c)$ resulting in considerable deviation from linearity in the fractal plot (R^2 = 0.9002). Fractal dimension measured from this plot was D = 1.25, an erroneous result.

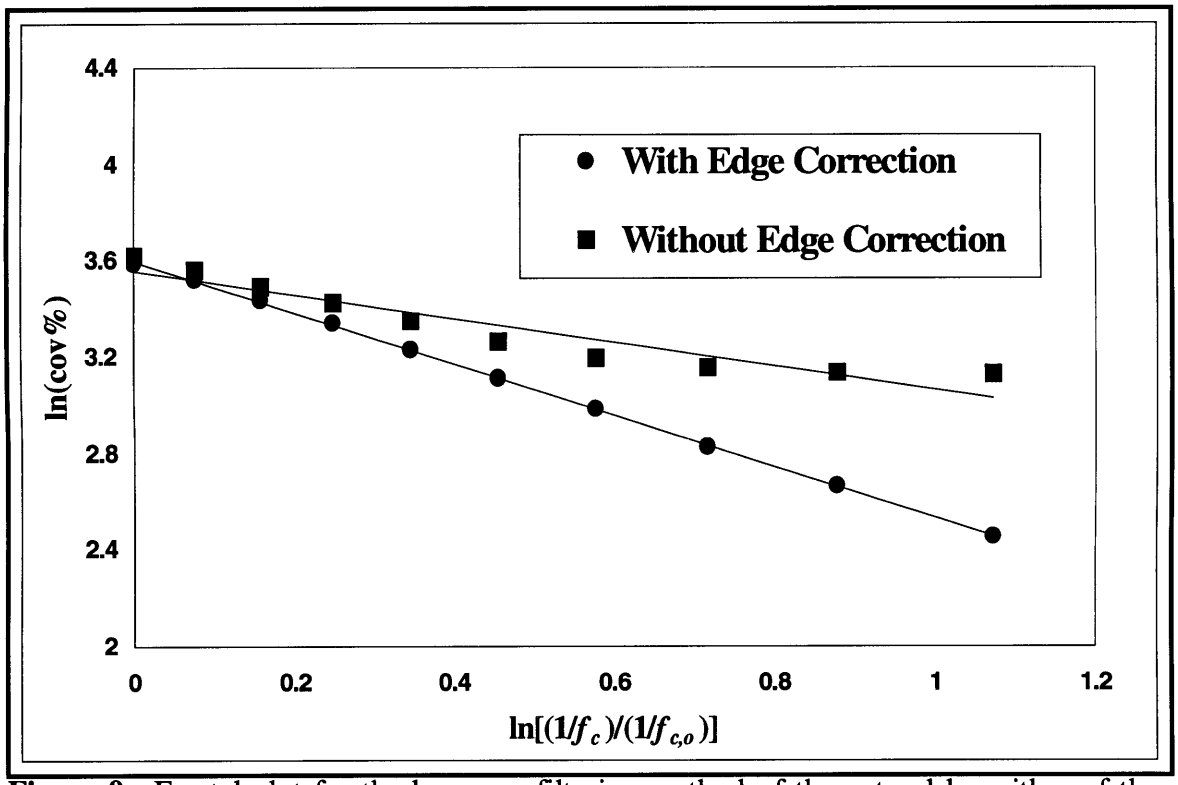

Figure 9. Fractal plot for the low-pass filtering method of the natural logarithm of the *cov* versus the natural logarithm of the normalized inverse corner frequency of the filter. Method was applied to a random noise image that was corrected for edge-smearing (normalization by an equivalently filtered unity mask) at each level of resolution (•). The expected linearity (R^2 = 0.9997) and fractal dimension (D = 1.53) are calculated from the best-fit line. Without correction for smeared edges (■), increasing resolution scale introduces artifactual heterogeneity that causes deviation from linearity (R^2 = 0.9002) and an erroneous fractal dimension (D = 1.25).

Plateau in the Fractal Plot. Using the low-pass filtering method, we observed a plateau in ln(*cov*%) for decreasing resolution scales ($\ln[(1/f_c)/(1/f_{c,o})]$). The point of plateau occurred at the same resolution scale for all images studied (figure 8). Fractal analyses has been proposed as a means to identify the functional unit of perfusion by finding the piece size where the *cov* inflects towards a plateau in the fractal plot [5]. For this identification, however, it is required for the smallest resolution scale to be smaller than the size of the functional unit and that the grid used is not misregistered with the governing fractal pattern. The fact that Glenny and Robertson did not observe a plateau in their fractal analyses of six dogs suggests that the size of the functional unit of perfusion could smaller than 24 mm^3 [5]. In our analyses, the observed point of plateau cannot reflect the functional unit of perfusion since our smallest resolution scale (7 mm × 7 mm × 6 mm) was larger than 24 mm^3. The point of plateau in figure (8) took place at a corner frequency corresponding to the spatial resolution of the PET camera (7 mm). Further decreases in resolution scale by increasing low-pass filter corner frequencies showed no change in the measured heterogeneity because the maximum resolution limit of the camera had been reached.

The Effect of Large Scale Perfusion Gradients on the Estimate of D. The average fractal dimension for pulmonary perfusion in our dogs was 1.31, whereas Glenny and Robertson report a somewhat smaller average fractal dimension of 1.09 for dogs [5]. We theorize that this difference could be explained by the vertical gradients in perfusion observed in supine dogs. These gradients were removed from our images before analysis, and not from the microsphere perfusion measurements of Glenny and Robertson. From equation (4), *D* can be interpreted as a measure of the relative reduction

in *cov* as length scale is increased and thus a reflection of the relative contribution of the different length scales to the spatial heterogeneity in perfusion. Systematic whole lung gradients in perfusion correspond to large length scales, and therefore their contribution to overall spatial heterogeneity should weight D towards 1.0, which is the fractal dimension for perfect spatial homogeneity. We reanalyzed our six PET perfusion images with the low-pass filtering method, this time leaving the vertical gradients intact. This resulted in an average value for D of 1.12, much closer to the value reported in [5]. In this case, however, the average R^2 was reduced to 0.96, suggesting that low frequency perfusion gradients (e.g., dorsoventral) are not fractal in nature and thus offset the linearity between $\ln(\mathrm{cov}(f_c))$ and $\ln\left(\frac{1}{f_c}\right)$.

5. CONCLUSIONS

We have devised an alternative method to characterize fractal properties of functional images. Successive two-dimensional low-pass filtering of the images effectively changes spatial resolution and thus their heterogeneity. Resolution scale is inversely proportional to the corner frequency of the low-pass filter. The fractal dimension can be computed from the slope of the log-log plot of the coefficient of variation versus the inverse of the low-pass filter corner frequency. The method does not require the exclusion of peripheral perfusion data with increasing resolution scale and therefore ensures a robust measure of the fractal dimension. Moreover, the method is insensitive to the effects of misregistration.

6. APPENDIX: RELATIONSHIP BETWEEN FRACTAL DIMENSION AND POWER SPECTRAL DENSITY

From the fractal analysis described above, it became apparent that the fractal dimension of a functional image could be related to the power spectral density (PSD). We thus theorized that proportionality should exist between the mean-normalized variance (cov^2) of a low-pass filtered image and the integral of the PSD (expressed in polar coordinates) from the origin to the corner frequency f_c of the low-pass filter. A PET image can be considered as a three-dimensional function, say $z = f(x,y)$. The z-coordinate corresponds to local radioactivity concentration (proportional to perfusion). The x-y plane specifies the voxel location within the image. Any mathematical function can be approximated by a sum of a finite number of sinusoids of different frequencies. The PSD of a functional image measures the energy content at each of the frequencies present in that image. Mathematically, the hypothesis can be stated as:

$$\mathrm{cov}^2\Big|_{f_c} = \left(\frac{\sigma}{\bar{x}}\right)^2\Bigg|_{f_c} = K \times \int_{\vartheta=0}^{\vartheta=2\pi}\left[\int_{r=0}^{r=f_c} PSD(r,\vartheta)\,dr\right]d\vartheta \qquad \text{(A1)}$$

In this equation, K is the constant of proportionality, $r = \sqrt{x^2 + y^2}$ and $\vartheta = \tan^{-1}\sqrt{y/x}$. x and y are the spatial frequencies in rectangular coordinates for the PSD. r and ϑ thus define the polar coordinate grid for the PSD, and r corresponds to a radial frequency. A physical interpretation of equation (A1) is that the spatial heterogeneity remaining in an image after low-pass filtering it with corner frequency f_c should be proportional to the sum of the energy content up to that frequency. An advantage associated with this

possibility is that calculation of the PSD, via the two-dimensional Fast Fourier Transform (FFT), consumes less time than successive low-pass filtering.

We tested this hypothesis first on the random noise images described above. The noise images were processed with a series of low-pass filters of increasing f_c and their mean-normalized variance was calculated. The PSD was calculated as square of the magnitude of the Fourier coefficients of the normalized image divided by the number of nonzero voxels. The integral of the PSD (from radius zero to each of the corner frequencies of the low-pass filters) was computed thereafter. Plots of mean-normalized variance versus the integral of the PSD were then generated. A representative plot is provided in figure (A1), with an R^2 of 0.9993. The slope of the plot is the constant of proportionality K between $\mathrm{cov}^2\big|_{f_c}$ and $\iint PSD(r,\vartheta)drd\vartheta$, determined to be equal to 2.7326×10^{-5}. The cov^2 of the image after low-pass filtering it with corner frequency f_c is calculated via equation (A1), and the log-log plot of cov versus the inverse of corner frequency is created. A representative plot is depicted is figure (A2), and its slope is used to calculate a fractal dimension D from equation (4). For this random noise image, D is equal to 1.47 with an R^2 of 0.996.

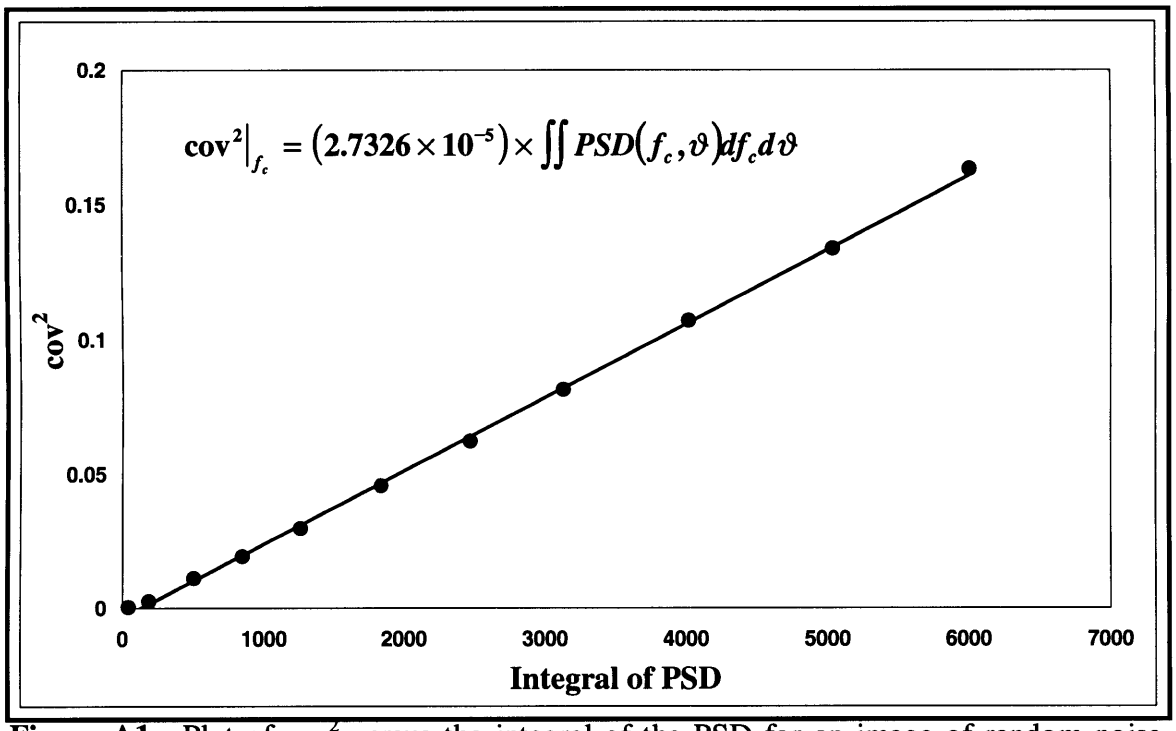

Figure A1. Plot of cov^2 versus the integral of the PSD for an image of random noise given the shape of a lung. The slope of this line is the constant of proportionality denoted K in equation (A1).

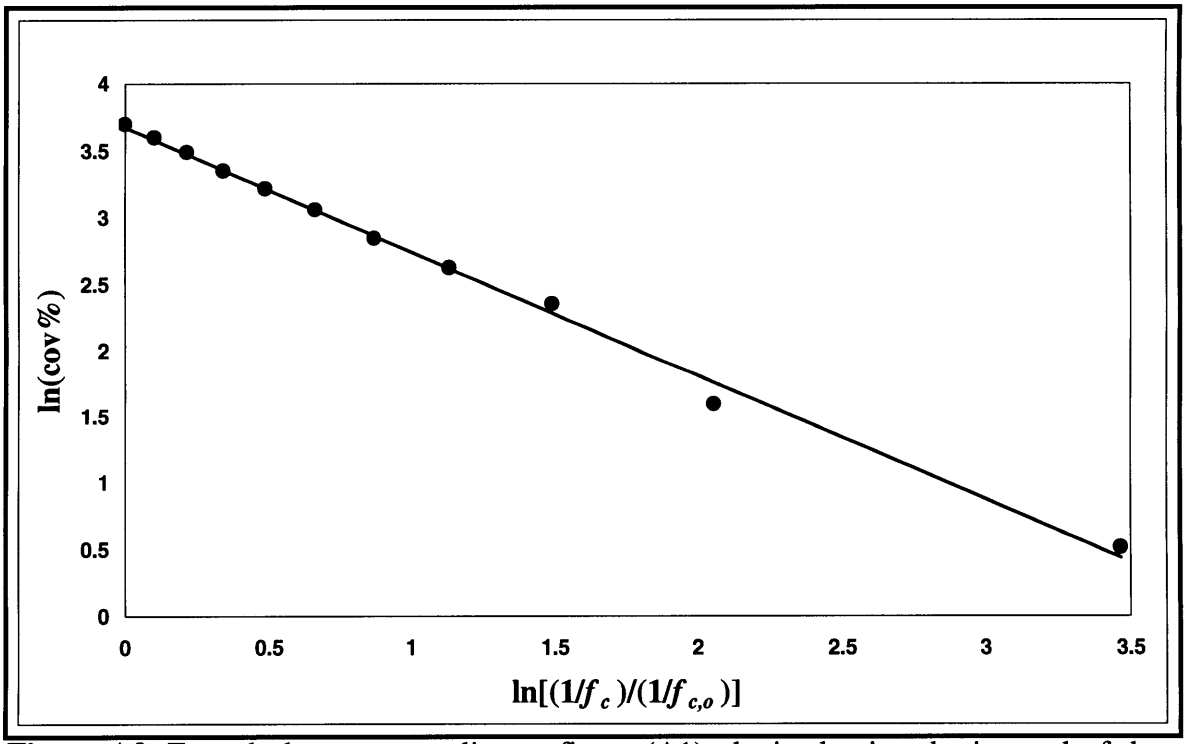

Figure A2. Fractal plot corresponding to figure (A1) obtained using the integral of the PSD. $D = 1.47$. $R^2 = 0.996$.

The linear relationship between $\text{cov}^2\big|_{f_c}$ and $\iint PSD(r,\vartheta)drd\vartheta$ is valid for images of random noise and provides a method to estimate their fractal dimension, which should have been 1.5 for perfect heterogeneity. Given these results we proceeded to use the PSD method to extract the D of PET images of pulmonary perfusion. A plot of $\text{cov}^2\big|_{f_c}$ versus $\iint PSD(r,\vartheta)drd\vartheta$ (figure A3) shows substantial deviation from linearity. The nonlinearity makes it no longer feasible to accurately assay D using the PSD method. We speculated that low frequencies remaining in the PET image, despite removing dorsoventral perfusion gradients, could be responsible for the failure.

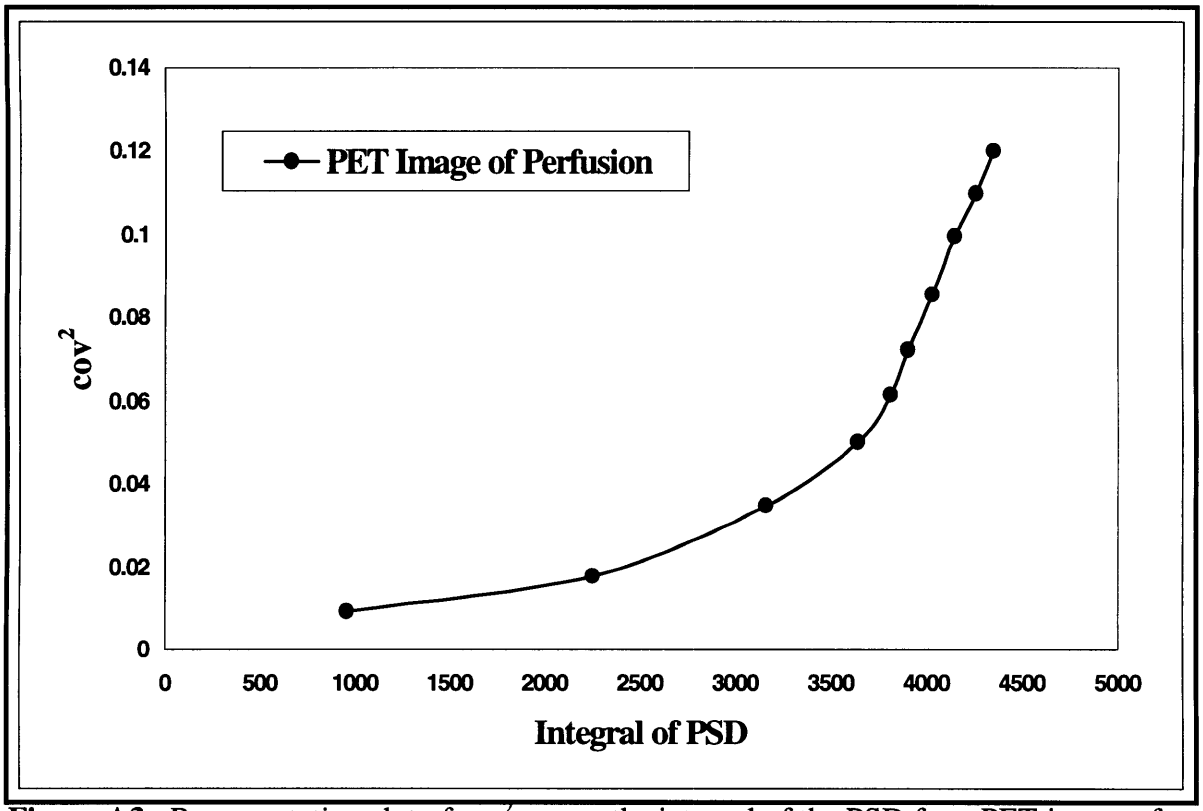

Figure A3. Representative plot of cov^2 versus the integral of the PSD for a PET image of perfusion (data taken from Dog 1). Note that the relationship predicted by equation (A1) is not valid.

Clearly, the PSD of noise (figure A4) shows monotonic increase in power with frequency. In contrast, the PSD of a perfusion image shows substantial components of lower frequencies that are not eliminated after removing the vertical gradients (figure A5). These frequencies include energy caused by the shape of the lung that is not included in the estimates of the *cov* after low-pass filtering.

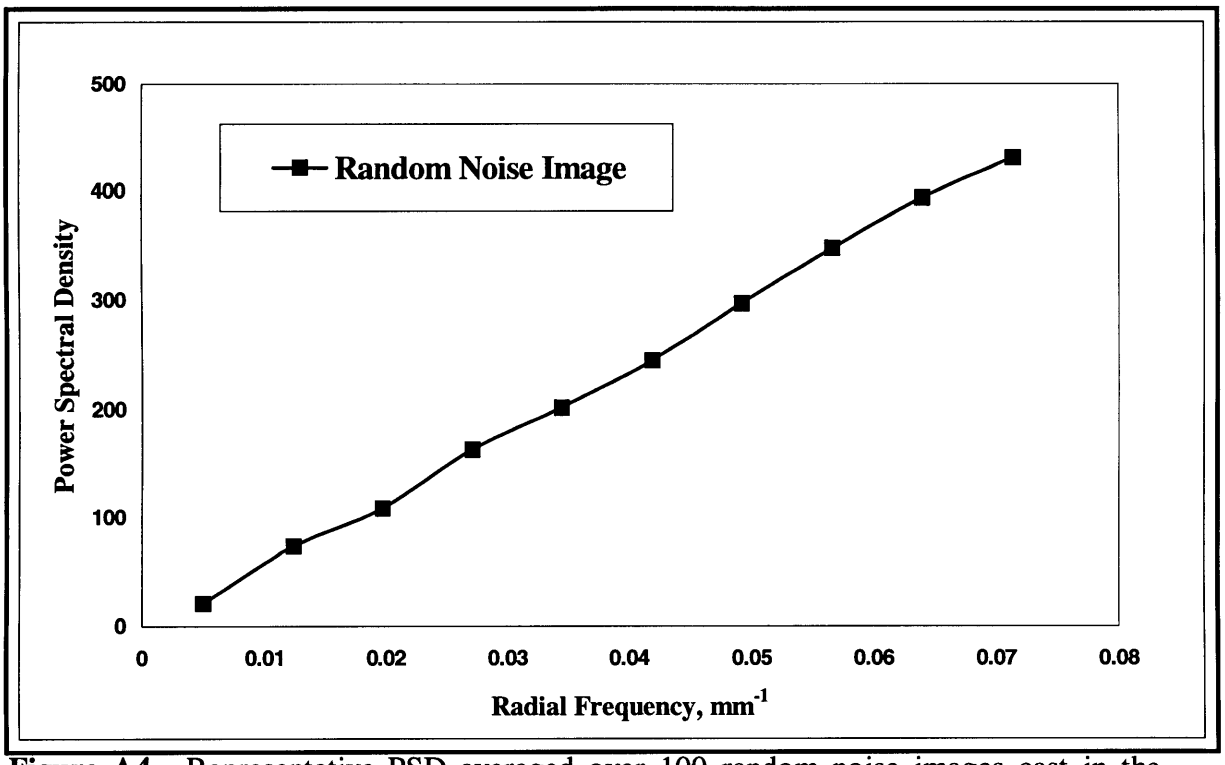

Figure A4. Representative PSD averaged over 100 random noise images cast in the shape of a lung. Dominant low frequency power is not present, as in figure (A5).

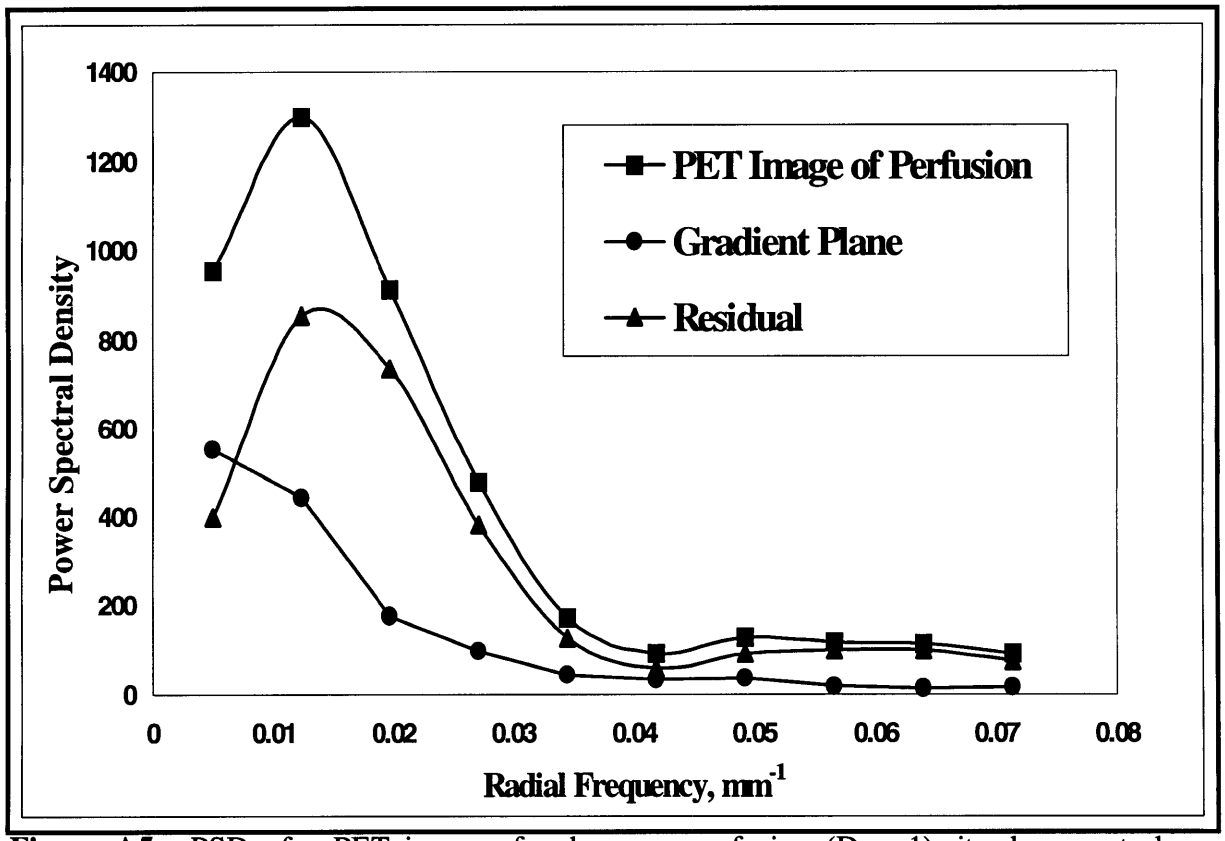

Figure A5. PSD of a PET image of pulmonary perfusion (Dog 1), its dorsoventral gradient plane, and the difference. Despite removing gradient planes with linear regression, physiologic low frequency power remains dominant in the PET image.

The hypothesis was further tested by superimposing a parabolic gradient on the same random noise image used in figure (A1) in the same direction of a real image dorsoventral perfusion gradient. A parabolic plane ($z = f(x,y) = y^2$) was calculated over the same 128×128 voxel grid as the perfusion image, and then multiplied by a unity mask to give it the shape of a lung. The polynomial image multiplied the noise image, creating the superimposition. Only the gradient vertical plane was removed from the superimposed image, analogous to removing dorsoventral perfusion gradients from the PET images. The low frequency remaining in the superimposed image shows the trend away from linearity when compared to the original image data (figure A6). The constant of proportionality K between $\mathrm{cov}^2\big|_{f_c}$ and $\iint PSD(r,\vartheta)drd\vartheta$ changed to 2.2167×10^{-5} and R^2 was reduced to 0.9919. The reduction in R^2 is consistent with the notion that low frequencies remaining after removing the gravitational gradient affect the relationship in equation (A1), making it nonlinear.

The lack of linearity in the relation of equation (A1) for PET functional images invalidates the use of the PSD approach to assess D. However, this work suggests that a proper power spectral density function of functional images can be obtained by means of the low-pass filtering method. This is done by calculating the difference in the cov^2 between a low-pass filtered PET image with two adjacent corner frequencies $f_{c,1}$ and $f_{c,2}$ ($f_{c,2} > f_{c,1}$), giving a measure of the spatial heterogeneity content within these frequencies.

Finally, this work suggests that the fractal dimension can be interpreted as a measure of the frequency content of the spatial heterogeneity.

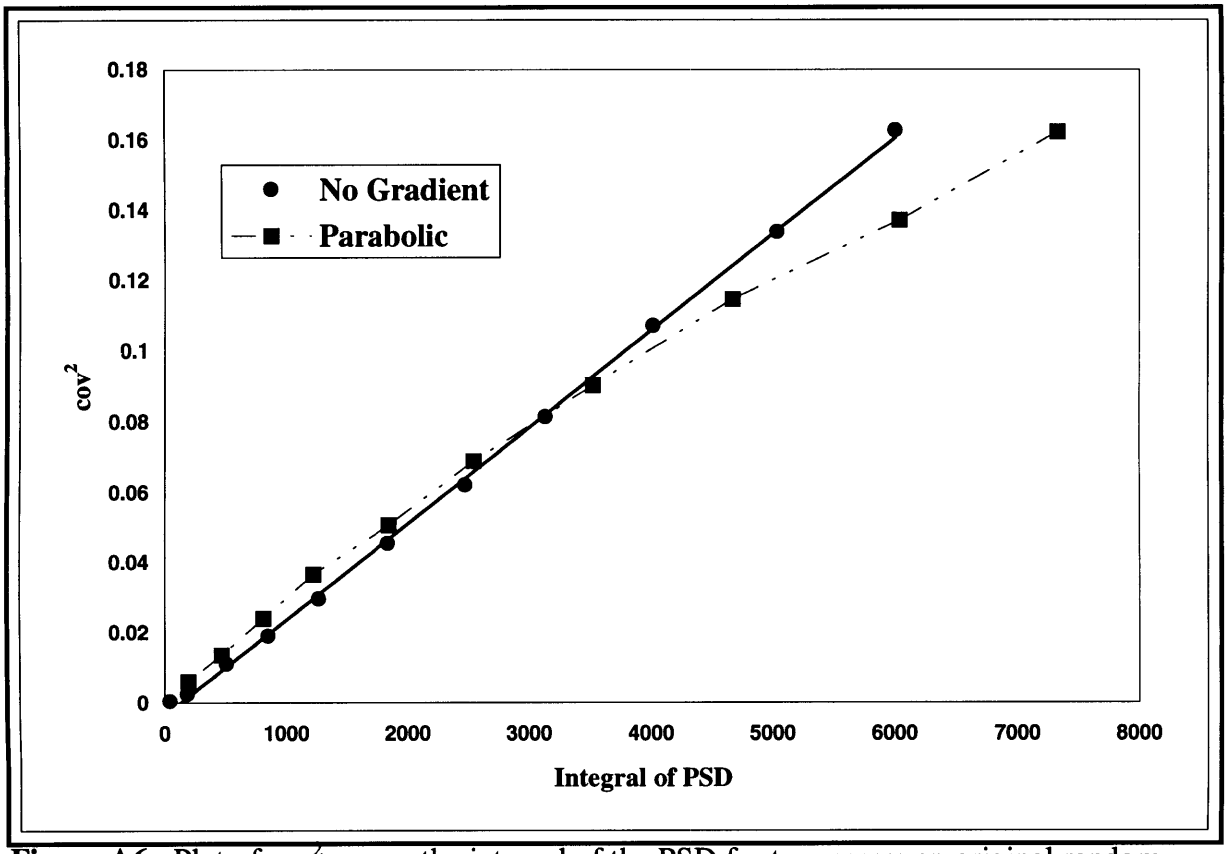

Figure A6. Plot of cov^2 versus the integral of the PSD for two cases: an original random noise image cast in the shape of the lung (•), and the same image superimposed with a parabolic gradient (■). The best-fit vertical gradient plane was removed from the superimposed image.

7. REFERENCES

[1] Bassingthwaighte, J.B., L.S. Liebovitch and J.B. West. *Fractal Physiology* (*Methods in Physiology 2 an American Physiological Society Book*). Oxford University Press. December, 1994.

[2] Galletti, G.G. and J.G. Venegas. Fractal Analysis of Positron Emission Tomograpy (PET) Images of Pulmonary Blood Flow (*Q*) (Abstract). *Am. J. Respir. Crit. Care Med.* 155, *Suppl.* 4, pt. 2: A743, 1997.

[3] Glenny, R.W., and H.T. Robertson. Fractal properties of pulmonary blood flow: characterization of spatial heterogeneity. *J. Appl. Physiol.* 69: 532-545, 1990.

[4] Glenny, R.W., and H.T. Robertson. Fractal modeling of pulmonary blood flow heterogeneity. *J. Appl. Physiol.* 70: 1024-1030, 1991.

[5] Glenny, R.W., H.T. Robertson, S. Yamashiro, and J.B. Bassingthwaighte. Applications of fractal analysis to physiology. *J. Appl. Physiol.* 1991.

[6] Mijailovich, S.M., Steven Treppo and Jose G. Venegas. Effects of lung motion and tracer kinetics corrections on PET imaging of pulmonary function. *J. Appl. Phsyiol.* 82: 1154-1162, 1997.